Herpes simplex virus 1 protein pUL21 stimulates cellular ceramide transport by activating CERT

Tomasz H. Benedyk[1,a], Viv Connor[1], Eve R. Caroe[2,b], Maria Shamin[2], Dmitri I. Svergun[3], Janet E. Deane[2], Cy M. Jeffries[3], Colin M. Crump[1], Stephen C. Graham[1]*

[1]Department of Pathology, University of Cambridge, Tennis Court Road, Cambridge, UK

[2]Cambridge Institute for Medical Research, University of Cambridge, Cambridge Biomedical Campus, Cambridge, UK

[3]European Molecular Biology Laboratory (EMBL) Hamburg Site, c/o DESY, Notkestrasse 85, Hamburg, Germany

[a]Current address: EG427 Pinpoint Gene Therapy, 29 Rue du Faubourg Saint-Jacques, Paris, France

[b]Current address: The Francis Crick Institute, 1 Midland Road, London, UK

***Corresponding author:** scg34@cam.ac.uk

ORCIDs: THB 0000-0001-6420-3665; ERC 0000-0003-3529-024X; MS 0000-0002-7291-2530; DIS 0000-0003-0830-5696; JED 0000-0002-4863-0330; CMJ 0000-0002-8718-7343; CMC 0000-0001-9918-9998; SCG 0000-0003-4547-4034

Short title: HSV-1 pUL21 modulates cellular ceramide transport

Contributions: Conceptualization: SCG; Data Curation: THB, CMJ, SCG; Funding Acquisition: JED, CMC, SCG; Investigation: THB, VC, ERC, MS, CMJ, CMC, SCG; Project Administration: SCG; Resources: DIS, JED; Supervision: CMC, SCG; Visualization: THB, SCG; Writing – Original Draft Preparation: THB, SCG; Writing – Review & Editing: THB, JED, CMJ, CMC, SCG.

Abstract

Herpes simplex virus (HSV)-1 dramatically alters the architecture and protein composition of cellular membranes during infection, but its effects upon membrane lipid composition remain unclear. HSV-1 pUL21 is a virus-encoded protein phosphatase adaptor that promotes dephosphorylation of multiple cellular and virus proteins, including the cellular ceramide transport protein CERT. CERT mediates non-vesicular transport of ceramide from the ER to the *trans*-Golgi network, whereupon ceramide is converted to sphingomyelin and other sphingolipids that play important roles in cell proliferation, cell signalling and membrane trafficking. Using click chemistry to profile the kinetics of sphingolipid metabolism in cultured cells, we show that pUL21-mediated dephosphorylation activates CERT and increases the rate of ceramide to sphingomyelin conversion. Purified pUL21 and full-length CERT interact with sub-micromolar affinity and we map the domains responsible for the interaction. Solving the solution structure of the pUL21 C-terminal domain in complex with the CERT PH and START domains using small-angle X-ray scattering allows us to identify a single amino acid mutation on the surface of pUL21 that disrupts CERT binding *in vitro* and in cultured cells. Sphingolipid profiling demonstrates that ceramide to sphingomyelin conversion is severely diminished in the context of HSV-1 infection, a defect that is compounded when infecting with a virus encoding the mutated form of pUL21 that lacks the ability to activate CERT. However, virus replication and spread are not significantly altered when pUL21-mediated CERT dephosphorylation is abolished, highlighting that dephosphorylation of other cellular and/or viral targets underpins the important role of pUL21 in HSV-1 biology.

Significance

Herpes simplex virus (HSV)-1 causes a life-long dormant infection of neurons, sporadically reactivating to manifest as cold-sores or genital herpes. While the impact of HSV-1 upon the protein content of infected cells has been well studied, we know relatively little about its impact upon cellular lipids. Using bioorthogonal labelling in cultured cells we show that HSV-1 protein pUL21 activates the key cellular lipid transport protein CERT to accelerate the conversion of ceramide to sphingomyelin. HSV-1 infection dramatically alters the kinetics of ceramide metabolism, leading to ceramide accumulation. Mutation of HSV-1 pUL21 to prevent CERT activation further enhances ceramide accumulation but this does not alter the replication or spread of HSV-1, highlighting that other cellular and/or viral proteins represent the critical targets of pUL21-mediated dephosphorylation in cultured cells.

Introduction

Herpes simplex virus (HSV)-1 is a human pathogen that is estimated to infect the majority of the human population, causing a life-long latent infection [1]. Latent HSV-1 resides in sensory or sympathetic neurons, migrating to the periphery in periodic reactivation events throughout the lifetime of the host. In order to sustain acute (lytic) infection, HSV-1 drastically modifies infected cells [2–5]. In particular, the virus extensively remodels the composition and architecture of cellular membranes to facilitate virus assembly and spread. Nascent capsids leave the nucleus via sequential envelopment and de-envelopment at the inner and outer nuclear membranes [6]. These cytosolic capsids acquire a proteinaceous layer termed 'tegument' and bud into the lumen of post-Golgi membranes that are studded with viral glycoproteins (so called 'secondary envelopment') [7]. The resultant virus-containing vesicles are transported to cell contact sites where they release the mature virus particles to disseminate the infection [8].

HSV-1 pUL21 is a tegument protein that is conserved in all alphaherpesviruses [9]. This multifunctional protein and its homologues are known to interact with multiple cellular and viral partners, including pUL16 [10,11], pUL11 [12], gE [12], tubulin [13] and Roadblock-1 [14], and it has been implicated in a number of important processes including capsid nuclear egress [15], viral cell-to-cell spread [12,16], and retrograde transport along axons to the neuronal cell bodies where latency is established [14,17]. Mutant HSV-1 lacking pUL21 expression exhibits a 10- to 100-fold replication defect and severely impaired cell-to-cell spread, both of which can be at least partially ascribed to the phosphomodulatory role of pUL21 as a protein phosphatase 1 (PP1) adaptor [18]. PP1 is a highly active and abundant cellular phosphatase [19] and pUL21 recruits PP1 to promote dephosphorylation of multiple substrates, including the viral protein pUL31 that is implicated in viral nuclear egress [18,20] and the cellular protein CERT that regulates sphingomyelin metabolism [18].

The cytoplasmic ceramide transport protein CERT (a.k.a. Goodpasture's antigen binding protein, GPBP, encoded by the gene *COL4A3BP*) mediates the non-vesicular trafficking of ceramide from the endoplasmic reticulum (ER) to the *trans*-Golgi network (TGN) and, in doing so, defines the rate of sphingomyelin synthesis [21–23]. CERT contains two well-folded globular domains: an N-terminal pleckstrin homology (PH) domain that mediates its interaction with TGN membranes by binding phosphatidylinositol 4-phosphate, and a C-terminal steroidogenic acute regulatory related lipid transfer (START) domain that directly binds ceramide to mediate its transfer [23]. Crystal structures of both domains have been solved [24,25]. The 'middle region' (MR) that connects the PH and START domains of CERT does not adopt a globular fold, instead containing a coiled-coil region that is likely to mediate CERT self-association [26], a 'two phenylalanines in an acidic tract' (FFAT) motif that recruits CERT to the ER membranes via binding proteins VAPA and VAPB [27], and a serine-rich motif (SRM), hyperphosphorylation of which represses CERT activity [28]. In cultured HeLa cells the vast majority of CERT is in an inactive, hyperphosphorylated state ($CERT^{P}$), available to be mobilised via dephosphorylation to increase the rate of ER-to-TGN ceramide transport in response to stimuli such as sphingomyelin depletion [28].

87 Ceramide (Cer) and sphingolipids like sphingomyelin (SM) are essential for mammalian cell growth and
88 they play important roles in cell signalling, apoptosis and membrane trafficking [29]. Furthermore,
89 sphingolipids and cholesterol participate in the formation of membrane microdomains (including 'lipid
90 rafts') that compartmentalise the lipid and protein composition of cellular membranes [30]. This
91 compartmentalisation is especially important in highly polarised cells such as neurons [31]. Although
92 sphingolipids are crucial to host-cell biology, relatively little is known about the interaction between
93 pathogens and cellular sphingolipid metabolism. The bacteria *Chlamydia trachomatis* is known to
94 directly recruit CERT to bacteria-containing intracellular inclusions, thereby increasing the abundance
95 of SM in the inclusion membrane [32], and CERT activity is necessary for the biosynthesis of double-
96 membrane vesicles that serve as the sites of hepatitis C virus and polio virus replication [33]. However,
97 to the best of our knowledge, the binding of CERT to HSV-1 pUL21 [18] is the only known example of
98 a direct interaction between CERT and a virus protein.

99 Previous studies have shown that HSV-1 infection increases Cer synthesis [34] and that depletion of
100 sphingomyelinase causes a >30-fold decrease in HSV-1 replication [35]. Sphingomyelinase treatment
101 of cultured epithelial cells has only a very modest effect upon HSV-1 entry [36], suggesting that SM is
102 not absolutely required for virus infection. In contrast, recent studies in macrophages demonstrated that
103 acid ceramidase activity is potently antiviral, helping sequester incoming virus particles by promoting
104 their neutralising association with sphingosine-rich intraluminal vesicles within endocytic multi-vesicular
105 bodies [37]. Furthermore, siRNA depletion of CERT has been shown to promote secretion of usually
106 cell-associated HSV-1 virions [38]. It is therefore increasingly clear that cellular sphingolipid metabolism
107 is important for HSV-1 biology, and that further studies are required to obtain a full picture of how specific
108 sphingolipids support and/or prevent HSV-1 infection.

109 We sought to define the functional consequences of the pUL21:CERT interaction for HSV-1 infection.
110 Using click-chemistry we demonstrated that pUL21-mediated CERT dephosphorylation increases the
111 rate of Cer to SM conversion in cultured cells. We characterised the solution structure of the pUL21 C-
112 terminal domain in complex with the PH and START domains of CERT, identifying a specific pUL21
113 amino acid required for the interaction. Functional characterisation of mutant HSV-1 encoding this
114 mutated form of pUL21 confirmed that pUL21-mediated CERT dephosphorylation alters the rate of SM
115 synthesis in infected cells. Furthermore, we observed a dramatic increase in the rate of Cer synthesis
116 in infected cells, which was only partly counteracted by pUL21-stimulated CERT activity, but this
117 increase in Cer abundance does not significantly alter virus replication or spread.

118 **Results**

119 Human cells typically maintain lipidome homeostasis via robust feedback and control mechanisms,
120 which respond to perturbations via local activation of specific signalling pathways [39,40]. We
121 hypothesised that pUL21, expressed at late points of infection [3], would likely alter the rate of
122 sphingolipid synthesis and thereby affect lipid-mediated signalling events, rather than altering the
123 overall steady-state lipid composition of infected cells. Synthetic lipids with alkyne-containing acyl
124 chains are efficiently processed by mammalian lipid-modifying enzymes and represent powerful tools
125 to probe lipid metabolism [41]. The impact of pUL21-directed CERT dephosphorylation on sphingolipid
126 metabolism was therefore probed using a clickable analogue of sphingosine (Sph), alkyne-Sph, to
127 monitor the rate of sphingomyelin biogenesis in immortalized human keratinocyte (HaCaT) cells.
128 Exogenous Sph is efficiently incorporated into cellular metabolic pathways, being rapidly converted into
129 ceramide (Cer) and then sphingomyelin (SM) or hexosylceramides (HexCer) like glucosylceramide or
130 galactosylceramide [42]. It is also converted into phosphatidylcholine (PC) via a so-called 'salvage'
131 pathway (Fig 1A) that directs sphingosine to palmitoyl-CoA which serves as substrate for re-acetylation
132 of lysophosphatidylcholine [43].

133 To monitor Sph metabolism, HaCaT cells, either parental or stably expressing pUL21 (HaCaT21), were
134 incubated with alkyne-Sph for five minutes (pulse) and the rate of alkyne-Sph incorporation into the
135 competing metabolic pathways was monitored for two hours (chase) by high performance thin layer
136 chromatography (HPTLC) separation and detection of lipids conjugated to coumarin-azide via a 'click'
137 reaction (Fig 1B and 1C). Alkyne-Sph was very efficiently converted to alkyne-Cer in both cell types,
138 the levels of alkyne-Cer remaining relatively stable throughout the chase, and for both cell types
139 synthesis of alkyne-PC and alkyne-SM was observed, but not synthesis of alkyne-HexCer. HaCaT21
140 cells exhibited significantly reduced rates of alkyne-Sph conversion and the level of alkyne-Cer is
141 significantly lower (Fig S1). The rate of alkyne-PC synthesis was also reduced, although this reduction
142 was not significant owing to the high inter-experiment variability of the alkyne-PC signal for the parental
143 HaCaT cells. Taken together, these results indicated that lipid metabolism is altered in HaCaT cells
144 constitutively expressing pUL21. However, it remained unclear whether these differences reflected
145 adaptations of cellular lipid metabolism in response to constitutive pUL21 expression rather than a direct
146 effect upon CERT activity. Since CERT-mediated non-vesicular transport of Cer from the ER to the
147 TGN defines the rate of Cer-to-SM conversion [21–23], pUL21-directed CERT dephosphorylation (and
148 thus activation) should increase the rate of SM synthesis. Consistent with this hypothesis, the
149 abundance alkyne-SM as a fraction of total alkyne-Cer plus alkyne-SM was significantly higher in
150 HaCaT21 versus HaCaT cells at early time points (0–30 min) during the chase (Fig 1D). By the 60 min
151 chase time point the rate of alkyne-SM accumulation slows and the difference in relative abundance
152 between cell lines was diminished, consistent with the alkyne-SM levels in both cell types approaching
153 equilibrium. This increase in alkyne-SM accumulation as a fraction of alkyne-Cer plus alkyne-SM
154 abundance was observed despite similar overall signal for alkyne-SM and alkyne-Cer in HaCaT21 cells
155 when compared to parental cells at early time points (0–30 min), the abundance of these lipids being
156 significantly lower in HaCaT21 cells at later time points (Fig 1E). Reduced overall levels of SM plus Cer

157 in HaCaT21 cells likely results from adaptation to constitutive pUL21 expression (and thus constitutive
158 CERT hyperactivation) via stimulation of feedback pathways that reduce Sph to Cer conversion and/or
159 increased back-conversion of SM and/or Cer to Sph. Treatment of HaCaT cells with the highly-specific
160 CERT inhibitor HPA-12 [44] confirmed that the rate of Cer-to-SM conversion was defined by CERT
161 activity: SM synthesis was significantly decreased in HPA-12–treated cells when compared with
162 untreated cells, and there was concomitant accumulation of alkyne-Cer in treated cells (Fig 1B–D and
163 Fig S1). Immunoblot analysis of protein samples that were re-solubilized following their precipitation
164 during lipid extraction (Fig 1F) confirmed that pUL21 was expressed and that dephosphorylated CERT
165 ($CERT^{O}$) predominates in HaCaT21 cells, in contrast to the parental and HPA-12 treated HaCaT cells.

166 pUL21 has multiple functions during infection, promoting the PP1-mediated dephosphorylation of not
167 just CERT but of multiple different cellular and viral proteins [18]. It was therefore essential to identify a
168 point mutant of pUL21 with impaired binding to CERT, but not to other cellular or viral partners, to
169 dissect the functional significance of increased CERT activity during infection. Defining the interaction
170 surfaces of transient protein complexes presents a considerable challenge [45], made more difficult in
171 the case of pUL21 and CERT by their containing multiple domains and regions of intrinsic disorder [18].
172 The minimal region of CERT required for pUL21 binding was thus probed using pull-down experiments
173 where pUL21-GST purified following bacterial expression (bait) was used to capture CERT or
174 truncations thereof (preys) expressed by *in vitro* coupled transcription/translation in wheat germ extract
175 (Fig 2A). The longer cytoplasmic isoform of CERT ($CERT_L$), where expression of exon 11 extends the
176 amino terminal region of the START domain by 26 amino acids ($START_L$), was used since both CERT
177 and $CERT_L$ have been shown to possess ceramide transfer activity [23] and a contribution of these
178 additional 26 amino acids to pUL21 binding could not be excluded. Full-length $CERT_L$ was efficiently
179 captured by pUL21-GST. The PH and $START_L$ domains were also captured by pUL21-GST when
180 expressed individually, albeit less efficiently, suggesting that the $CERT_L$ possesses multiple pUL21-
181 binding motifs. The CERT middle region, MR, was not captured by pUL21-GST and is thus likely to be
182 dispensable for binding. A truncated $CERT_L$ construct that retained the pUL21-binding PH and $START_L$
183 domains, but lacked the majority of the highly flexible MR, was thus designed for use in subsequent
184 biochemical and structural studies (mini$CERT_L$) (Fig 2B). The extent of the MR retained to link the two
185 domains was informed by the crystal structure of the CERT PH:START domain complex [46], defining
186 a minimal distance of at least 55 Å between the PH domain C terminus and the START domain N
187 terminus, and the desire to exclude the predicted coiled-coil region that may cause oligomerisation [26].
188 MR residues 132–350 were thus excluded from mini$CERT_L$. The first 19 amino acids of the PH domain
189 were also omitted from mini$CERT_L$ as this region is predicted to be highly disordered and was excluded
190 in previous structural studies [24,47].

191 Previous studies identified that the MR mediates CERT trimerisation [26,48]. Size-exclusion
192 chromatography with inline multi-angle light scattering (SEC-MALS) (Fig 2C) confirmed that
193 hyperphosphorylated StrepII-tagged $CERT_L^P$, purified following expression in mammalian (Freestyle
194 293F) cells, has an observed mass (184.3 kDa) approaching that expected for a trimer (215.7 kDa).
195 Similarly, a constitutively hypophosphorylated form of $CERT_L$ where S132 is mutated to alanine, and

196 thus cannot become phosphorylated to initiate the SRM phosphorylation cascade [28], had an observed
197 mass (199.2 kDa) approaching that expected for a trimer. In contrast, H_6-miniCERT$_L$ purified following
198 bacterial expression was predominantly monomeric and monodisperse (observed mass 43.9 kDa,
199 expected monomeric mass 44.9 kDa), consistent with trimerization of CERT$_L$ being driven by the MR
200 and not being dependent upon CERT$_L$ phosphorylation.

201 Isothermal titration calorimetry (ITC) demonstrated that pUL21 binds CERT$_L$ with approximately
202 micromolar affinity (Fig 2D,E and Table 1), the observed affinity not differing significantly between the
203 hyperphosphorylated (CERT$_L^P$) and hypophosphorylated (CERT$_L^{S132A}$) forms of the protein. While
204 CERT$_L^{S132A}$ forms a 1:1 complex with pUL21, the observed binding stoichiometry (N) was consistently
205 lower for CERT$_L^P$ (0.74), consistent with a proportion of the pUL21 binding sites on CERT$_L$ being
206 sterically occluded when the protein is hyperphosphorylated. MiniCERT$_L$ and pUL21 form an equimolar
207 complex, binding with micromolar affinity similar to the full-length protein (Fig 2F; Table 1). However,
208 the thermodynamics of binding differ significantly; whereas pUL21 binding to CERT$_L$ is endothermic
209 and entropically driven, binding to miniCERT$_L$ is exothermic and enthalpically driven with minimal
210 change in overall entropy (Table 1). This is consistent with CERT$_L$ undergoing significant conformational
211 rearrangement upon binding to pUL21, whereas the conformational changes to miniCERT$_L$ (if any) upon
212 pUL21 binding are likely to be much more modest.

213 Small-angle X-ray scattering (SAXS) in batch mode was used to probe the solution structure of H_6-
214 miniCERT$_L$ (Fig 2G; Table S1). The frequency distribution of real-space distances ($p(r)$ profile) is largely
215 symmetric (Fig 2H) and the dimensionless Kratky plot (Fig 2I) has a bell-shaped peak at $sR_g = \sqrt{3}$,
216 consistent with miniCERT$_L$ having a compact globular conformation in solution. *Ab initio* modelling of
217 the H_6-miniCERT$_L$ scattering profile using GASBOR [49] yields a dummy-residue model (Fig 2J,K) that
218 closely resembles the crystal structure of CERT START and PH domain complex [46]. A pseudo-atomic
219 model of the H_6-miniCERT$_L$ solution structure, generated using the crystal structures of the CERT PH
220 and START domains determined in isolation [24,25] as rigid bodies, closely resembles the crystal
221 structure of the CERT PH:START domain complex (Fig 2L,M). Collectively, the MALS, ITC and SAXS
222 analysis demonstrates that miniCERT$_L$ forms a compact monomeric protein with high affinity for pUL21,
223 representing an excellent tool for structural studies.

224 Structural characterisation via X-ray crystallography and SAXS has revealed pUL21 to comprise two
225 domains joined by a highly flexible linker [18,50,51], and immunoprecipitation experiments mapped
226 CERT binding to the pUL21 C-terminal domain [18]. The C-terminal domain of pUL21 (pUL21C),
227 spanning amino acids 275–535, was expressed with a hexahistidine tag and purified following bacterial
228 expression. In contrast to a previous report [50] we did not observe co-purification of nucleic acid with
229 H_6-pUL21C, the purified protein having an $A_{260/280}$ ratio of ~0.6. SAXS analysis (Fig S2) confirmed that
230 H_6-pUL21C is monomeric and monodisperse, adopting a compact structure in solution that matches
231 the previously determined crystal structure ($\chi^2 = 0.99$, CorMap p = 0.133) [50]. SEC analysis of a pre-
232 formed complex between purified H_6-miniCERT$_L$ and a 1.34-fold molar excess of H_6-pUL21C confirmed
233 that the two proteins form a stable complex (Fig 3A), suitable for structural studies. ITC demonstrated

234 that H_6-pUL21C forms an equimolar complex with H_6-miniCERT$_L$ with a dissociation constant (K_D) of
235 4.3 ± 1.2 μM (Fig 3B; Table 1). The approximately 4-fold reduction in miniCERT$_L$ binding by pUL21C
236 versus full-length pUL21 is consistent with previous immunoprecipitation results, where transfected
237 pUL21C-GFP captured endogenous CERT slightly less efficiently than did pUL21-GFP in HEK293T
238 cells [18]. These ITC experiments confirm that the C-terminal domain of pUL21 is the major determinant
239 of CERT binding.

240 To probe the structural basis of the CERT recruitment by pUL21, a pre-formed complex of H_6-
241 miniCERT$_L$ and H_6-pUL21C was subjected to SEC with inline SAXS measurement (SEC-SAXS, Fig
242 3C). SAXS data were processed by averaging frames with a consistent calculated radius of gyration
243 (R_g) and then subtracting averaged buffer frames to yield the H_6-miniCERT$_L$:H_6-pUL21C complex
244 scattering profile (Fig 3D). The probable frequency of real-space distances ($p(r)$ profile) of the complex
245 is moderately asymmetric (Fig 3E), in contrast to the highly symmetric $p(r)$ profiles of H_6-pUL21C (Fig
246 S2B) or H_6-miniCERT (Fig 2H) alone, suggesting a less spherical particle, and the dimensions of the
247 complex (R_g 3.5 nm, D_{max} 13.6 nm) are substantially larger than for H_6-pUL21C (R_g 2.2 nm, D_{max} 8.5
248 nm) or H_6-miniCERT (R_g 2.7 nm, D_{max} 9.1 nm). The peak of the dimensionless Kratky plot is slightly
249 higher, with its peak away from $sR_g = \sqrt{3}$ (Fig 3F), suggesting some flexibility in the system granted
250 either by modest dissociation of the complex or some mobility of the H_6-miniCERT$_L$ domains with
251 respect to each other and H_6-pUL21C. *Ab initio* modelling using GASBOR indicated an elongated
252 molecule (Fig 3G). While initial pseudo-atomic models of the complex generated using a fixed
253 conformation of H_6-miniCERT$_L$ did not fit the SAXS profile acceptably, allowing the PH and START$_L$
254 domains freedom to move with respect to each other and to H_6-pUL21C yielded three pseudo-atomic
255 models with high-quality fits to the SAXS profile (Fig 3H and Fig S3). In all three top models miniCERT$_L$
256 binds 'end-on' to the pUL21 molecule, forming an ellipsoidal 'rugby ball' like particle. In two of the top
257 three models miniCERT$_L$ binds the 'left wing' of the dragonfly-shaped pUL21C domain [50], whereas in
258 the other it binds the 'right wing' (Fig S3). These models all have a similar overall shape, and thus all
259 explain the SAXS scattering data well, but the relative orientations of H_6-miniCERT$_L$ and H_6-pUL21C
260 differ. All three top models were thus used to design specific pUL21 mutations that might disrupt
261 (mini)CERT binding.

262 Mutations in pUL21C were designed to identify whether miniCERT$_L$ binds the left or right wing of this
263 domain. Amino acids in helix α4 or the subsequent loop of pUL21C were mutated to test binding to the
264 left wing (Fig 3H, Fig S3), whereas amino acids in helices α5 and α9 were used to test binding to the
265 right wing (Fig S3B). Immunoprecipitation experiments in transfected HEK293T cells that had been
266 infected with HSV-1 lacking pUL21 expression (HSV-1 ΔpUL21) demonstrated that 4 of 5 substitution
267 in the left wing of pUL21C (P365D, V368E, R373E and V382E) disrupted the ability of CERT to co-
268 precipitate with pUL21-GFP (Fig 4A), whereas none in the pUL21C right wing disrupted CERT co-
269 precipitation (Fig S3C). These results are consistent with CERT binding the left wing of pUL21C. The
270 proximity of the pUL21C amino terminus to miniCERT$_L$ in these models is also consistent with
271 observations that CERT binding is lost when pUL21C has a bulky N-terminal GFP tag, but retained
272 when the GFP tag is C-terminal [18].

273 Of the pUL21 substitutions that disrupted CERT binding (Fig 4A), V382E appeared to cause the largest
274 decrease in CERT binding while maintaining the ability of pUL21 to co-precipitate its other known
275 binding partners, PP1 [18] and pUL16 [10]. H_6-pUL21^{V382E} was purified following bacterial expression.
276 Differential scanning fluorimetry (a.k.a. Thermofluor) showed pUL21^{V382E} to be well folded as its thermal
277 stability is similar to wild-type H_6-pUL21 (Fig 4B). ITC analysis demonstrated that H_6-pUL21^{V382E} has
278 approximately 8-fold reduced binding affinity for H_6-miniCERT$_L$ when compared to wild-type pUL21 (Fig
279 4C; Table 1). The effect of the V382E substitution upon the ability of pUL21 to promote CERT
280 dephosphorylation, converting CERT^P to CERT^O, was probed using an *in vitro* dephosphorylation assay
281 with all-purified reagents (Fig 4D and E). The dose-dependent acceleration of GST-PP1 mediated
282 CERT dephosphorylation is significantly greater for wild-type pUL21 than pUL21^{V382E} ($p = 0.040$; two-
283 way ANOVA with Sidak's multiple comparison test), consistent with the GST-PP1:pUL21^{V382E} complex
284 having lower affinity for the substrate CERT^P (EC50[pUL21] = 0.491 ± 0.123 μM, EC50[pUL21^{V382E}] =
285 3.329 ± 0.7874 μM; three parameter dose-response curve, n = 2 independent experiments).

286 To probe the ability of pUL21^{V382E} to stimulate CERT dephosphorylation during infection, a mutant strain
287 of HSV-1 encoding pUL21^{V382E} was generated using two-step Red recombination [52].
288 Dephosphorylated CERT (CERT^O) is significantly less abundant in HaCaT cells infected with HSV-1
289 expressing pUL21^{V382E} or lacking pUL21 expression (ΔpUL21) when compared to wild-type HSV-1
290 infected cells (Fig 5A,B). In addition to CERT, pUL21 expression reduces the phosphorylation of
291 multiple substrates of the viral kinase pUS3 in HSV-1 infected cells [18], the phosphorylated forms of
292 these substrates being detectable using an antibody that recognises phosphorylated substrates of the
293 cellular kinase Akt [53]. While infection with ΔpUL21 HSV-1 causes a dramatic increase in the
294 abundance of multiple phosphorylated pUS3 substrates, the abundance of these phosphoforms is
295 indistinguishable between wild-type and pUL21^{V382E} HSV-1 (Fig 5A). This confirms that the V382E
296 substitution specifically disrupts CERT dephosphorylation, rather than generally inhibiting the ability of
297 pUL21^{V382E} to recruit PP1 to substrates. Similar changes in CERT dephosphorylation, but not in the
298 dephosphorylation of other pUS3 substrates, are observed when Vero cells are infected with pUL21^{V382E}
299 HSV-1 (Fig S4A,B). Immunocytochemistry confirms that both wild-type and V382E pUL21 have the
300 similar subcellular localisation, being observed predominantly at the nuclear rim of infected Vero cells
301 (Fig 5C).

302 Metabolic labelling was used to monitor the impact of pUL21-mediated CERT dephosphorylation on
303 sphingolipid biogenesis during infection. A pulse-chase experiment was performed where HaCaT cells
304 infected with wild-type or pUL21^{V382E} HSV-1, or mock infected, were incubated for 5 min with alkyne-
305 Sph at 14 hours post-infection (hpi) and its metabolites were monitored for two hours. Cer accumulates
306 and the rate of SM synthesis is significantly decreased in cells infected with wild-type and pUL21^{V382E}
307 HSV-1 when compared to uninfected cells (Fig 5D). Although a substantial decrease in the rate of SM
308 synthesis is seen for both wild-type and mutant HSV-1 infection, the defect is significantly larger in cells
309 infected with HSV-1 pUL21^{V382E} (Fig 5E). The overall abundance of SM plus Cer is similar between
310 infected and uninfected cells, suggesting that Cer to SM conversion is specifically impaired rather than
311 influx of click-Sph into the SM biogenesis pathway being defective (Fig 5F). Taken together, this

312 suggests that pUL21-mediated activation of CERT accelerates Cer to SM conversion during infection,
313 albeit from a much lower base than in uninfected cells.

314 Having confirmed that pUL21^{V382E} HSV-1 specifically lacks the ability to stimulate CERT
315 dephosphorylation, and that HSV-1 encoding pUL21^{V382E} has a reduced rate of Cer to SM conversion,
316 the impact of this deficit upon virus replication and spread in cultured cells was assessed. Wild-type
317 and pUL21^{V382E} HSV-1 form similar sized plaques on HaCaT and Vero cells (Fig 6A), suggesting that
318 CERT dephosphorylation is dispensable for efficient viral cell-to-cell spread. A single-step growth curve,
319 where Vero and HaCaT cells are infected at a high multiplicity of infection (MOI) and the production of
320 infectious progeny is monitored over time, was used to compare the replication of wild type and
321 pUL21^{V382E} HSV-1 (Fig 6B). Both viruses produce similar abundance of infectious progeny by 24 hours
322 post infection. In two biologically independent experiments performed for each cell type the kinetics of
323 virus replication was consistently accelerated, with higher titres of pUL21^{V382E} HSV-1 being observed
324 between 6–12 hours post-infection, but the difference in growth rate is not statistically significant for
325 either cell line (two-way ANOVA with Sidak's multiple comparisons test).

326 While HSV-1 preferentially remains cell-attached, spreading via direct cell:cell contacts, the cell-free
327 secretion of virions from infected cells is altered when CERT is depleted or overexpressed [54]. Cell-
328 free release of pUL21^{V382E} HSV-1 was determined by quantitating the amount of infectivity secreted into
329 the medium as a percentage of overall infectivity (secreted plus cell-associated), normalised for each
330 independent replicate to the secretion of a wild-type virus in control experiments performed at the same
331 time. HaCaT cells infected for 12 h with various MOI of pUL21^{V382E} HSV-1 did not release significantly
332 more or less infectivity when compared to WT HSV-1 infection (Fig 6C). Similarly, the cell-free release
333 of infectivity at 12 hpi did not differ between Vero cells infected with pUL21^{V382E} or WT HSV-1 (Fig S4C).

334

335 **Discussion**

336 HSV-1 extensively remodels the proteome of infected cells, altering both the abundance [3] and post-
337 translational modification status [2,18,55] of multiple cellular proteins. We know much less about HSV-1
338 mediated changes to the cellular lipidome, although previous studies have identified that HSV-1
339 infection changes phosphoinositide levels [56] and increases the rate of *de novo* phospholipid synthesis
340 [57]. By combining biochemical and structural studies with cell-based models of infection we show here
341 that pUL21 accelerates the conversion of Cer to SM in infected cells by promoting dephosphorylation
342 and activation of the Cer transport protein CERT (Fig 5). This is the first observation of a viral protein
343 directly binding CERT and altering its activity. While pUL21-mediated CERT activation causes an
344 apparent modest acceleration in the rate of virus replication, this effect is not statistically significant and
345 CERT activation does not contribute to replication or cell-to-cell spread of HSV-1 in cultured
346 keratinocytes or epithelial cells (Fig 6).

347 Our previous work showed that pUL21 is a phosphatase adaptor with multiple different targets [18].
348 Mutation of the pUL21 TROPPO motif, required for PP1 binding and thus stimulation of
349 dephosphorylation, dramatically reduced the replication and spread of HSV-1. While the TROPPO motif
350 was identified via its conservation across alphaherpesvirus sequences, the molecular basis of CERT
351 recruitment remained unknown. Biochemical mapping and SAXS structural characterisation allowed us
352 to identify a specific mutation, V382E, that decreases the affinity of pUL21 for miniCERT$_L$ by
353 approximately 8-fold (Fig 4C). While this reduction in affinity is moderate when assayed in dilute
354 biochemical solution, it is sufficient to disrupt co-precipitation of CERT from transfected cells (Fig 4A),
355 it abolishes pUL21-mediated dephosphorylation of CERT during infection (Fig 5A,B), and it significantly
356 increases the rate of Cer to SM conversion (Fig 5E). These results are consistent with other binding
357 partners competing to bind CERT and/or pUL21 within the context of infected cells, these competing
358 interactions amplifying the effect of reduced pUL21:CERT binding affinities. The V382E mutation does
359 not prevent pUL21 binding to pUL16 (Fig 4A) nor its ability to stimulate dephosphorylation of other
360 targets (Fig 5A), confirming that pUL21 binds CERT via a molecular surface that is distinct from the
361 binding site(s) of other targets. The wild-type levels of virus replication and cell-to-cell spread observed
362 for pUL21^{V382E} HSV-1 are consistent with our previous *in vitro* evolution studies of HSV-1 mutants where
363 the pUL21 TROPPO motif was mutated [18]. Adaptation of the virus to the loss of pUL21 PP1 binding,
364 via suppressor mutations that reduce the activity of the kinase pUS3, restored virus replication and
365 spread without restoring enhanced CERT dephosphorylation [18]. We therefore conclude CERT is not
366 a critical substrate of pUL21 for virus replication and spread in cultured fibroblasts and keratinocytes.
367 However, we note that HSV-1 is a neurotropic virus and that sphingolipids like SM are highly enriched
368 in neurons, where they are critical for correct neuronal development and function [31]. Studying the role
369 of pUL21-mediated CERT dephosphorylation in neurons thus remains an important question for future
370 investigation.

371 Studies of cellular lipid metabolism are complicated by robust cellular feedback mechanisms [58] and
372 challenges in accurately detecting changes in lipid abundance [59]. Here, we successfully employed

373 lipid labelling, click chemistry and HPTLC to monitor the kinetics of sphingosine metabolism, revealing
374 that HSV-1 pUL21 significantly increases the rate of CERT-mediated Cer to SM conversion both outside
375 (Fig 1) and within (Fig 5) the context of infection. Furthermore, we observe a highly significant increase
376 in the abundance of labelled Cer when cells are infected with HSV-1, this increase being greater when
377 pUL21-mediated CERT activation has been abolished. The dramatic change in the rate of Cer to SM
378 conversion is most likely explained by the known propensity of HSV-1 to promote dispersal of the Golgi
379 and TGN [4,60]. Such dispersal would alter ER:TGN contact sites, where CERT-mediated transport
380 enables Cer to SM conversion by TGN-resident sphingomyelin synthase [61].

381 HSV-1 utilizes the PKD-mediated trafficking from the TGN to the plasma membrane [62]. Disruption of
382 PKD-mediated trafficking has been shown to alter virus secretion, with siRNA-mediated depletion of
383 CERT increasing the secretion of extracellular (cell-free) HSV-1 particles and CERT overexpression
384 reducing virus secretion [54]. We do not observe changes in the secretion of pUL21^{V382E} HSV-1, which
385 lacks the ability to dephosphorylate CERT and thus activate CERT-mediated Cer transport. While these
386 results may appear at first glance to be contradictory, it should be noted that in our experiments the
387 cells contained wild-type levels of CERT and cells infected with either ΔpUL21 or pUL21^{V382E} HSV-1
388 have similar levels of active (CERT^{P}) and inactive (CERT^{O}) protein compared to uninfected controls
389 (Fig 5A). In contrast, siRNA depletion would lead to a complete absence of CERT and of CERT-
390 mediated lipid transfer. Furthermore, the previous study demonstrated that treatment of infected cells
391 with HPA-12 did not stimulate virus particle secretion [54]. This insensitivity of HSV-1 secretion to CERT
392 pharmacological inhibition, combined with our observation that pUL21-mediated CERT activation does
393 not alter HSV-1 secretion, strongly suggests that CERT catalytic activity is not directly linked to the
394 regulation of virus secretion.

395 Our observation of labelled Cer accumulation during HSV-1 infection (Fig 5) is consistent with an earlier
396 report that HSV-1 infection causes an approximately 2-fold increase in Cer abundance within BHK-21
397 cells [34]. Cer has many distinctive physical properties that set it apart from other membrane lipids: it
398 has negative intrinsic curvature, it increases the order of phospholipids in membranes, and it makes
399 biological membranes more permeable to even large solutes such as proteins [63]. Nascent HSV-1
400 particles must traverse multiple biological membranes during virus assembly, most notably during
401 capsid egress from the nucleus. Being too large to egress via nuclear pores, capsids leave by budding
402 into and then out of the perinuclear space, the former step being catalysed by the herpesvirus nuclear
403 egress complex (NEC) [64]. A recent study identified that the NEC induces lipid ordering to generate
404 the negative curvature required for capsid budding [65]. It is tempting to speculate that the accelerated
405 replication kinetics of pUL21^{V382E} HSV-1 arises, at least in part, from an increased rate of nuclear capsid
406 egress owing to increased Cer abundance. This effect would be distinct from the previously
407 demonstrated role of pUL21 in promoting nuclear egress via regulating the phosphorylation of NEC
408 components [18,20]. Increased Cer abundance could also stimulate secondary envelopment of virus
409 particles at post-Golgi membranes. However, in addition to potentially promoting virus assembly,
410 accumulation of Cer can lead to caspase 3 activation and apoptosis via increased mitochondrial outer
411 membrane permeabilization [66], and HSV-1 is known to encode proteins that defend against ceramide-

412 induced apoptosis [67]. It is therefore possible that pUL21-stimulated acceleration of Cer to SM
413 conversion acts to limit the pro-apoptotic activity of Cer, although confirmation of this requires further
414 study.

415 In summary, we demonstrated that pUL21 dephosphorylates and activates the cellular lipid transport
416 protein CERT, stimulating conversion of Cer to SM. Characterising the solution structure in complex
417 with the PH and START domains of CERT allowed us to identify a single amino acid mutation of pUL21
418 that disrupts CERT dephosphorylation in infected cells. HSV-1 encoding this pUL21 mutant had similar
419 replication kinetics, virus yields and plaque sizes, confirming that dephosphorylation of other cellular
420 and/or viral targets underpins the important role of pUL21 in HSV-1 replication and spread. The
421 functional rationale for pUL21-mediated modulation of CERT activity by HSV-1 remains elusive, but we
422 have defined the molecular tools that will allow its dissection in other cell types and/or animal models
423 of infection.

424

425 **Materials and methods**

426 *Plasmids*

427 The StrepII-CERT transient mammalian expression construct was described previously [18]. For
428 generation of stable cells, a synthetic gene encoding human $CERT_L$ (UniProt Q9Y5P4-1) was cloned
429 into a modified version of plasmid PB-T [68] that encodes an N-terminal StrepII tag and a woodchuck
430 hepatitis virus posttranscriptional regulatory element [69] in the 3′ untranslated region. The S132A
431 substitution was introduced into this vector using QuikChange mutagenesis (Agilent) according to the
432 manufacturer's instructions. $CERT_L$ destined for expression using *in vitro* transcription/translation
433 system from wheat germ extract was cloned into the plasmid pF3A WG BYDV (Promega) with an N-
434 terminal myc epitope tag. The truncations of $CERT_L$ were generated by inverse PCR (MR, residues
435 123–364; $START_L$, residues 365–624) or by introduction of a stop codon (PH, residues 1–122) using
436 QuikChange mutagenesis. For purification following bacterial expression, $miniCERT_L$ (residues 20–131
437 plus 351–624) was cloned into pOPTH [70], encoding a N-terminal MAH_6 tag. The generation of pUL21-
438 H_6 and pUL21-GFP were described previously [18] and single amino acid substitutions were introduced
439 by QuikChange mutagenesis. pUL21-H_6 was subcloned into pOPTH and inverse PCR was used to
440 generate H_6-pUL21C, encoding pUL21 amino acids 275–535. A plasmid (UK622) encoding mouse
441 PP1γ (UniProt P63087) with an N-terminal GST tag [71] was a kind gift from David Ron (Cambridge
442 Institute for Medical Research). To generate $pUL21^{V382E}$ HSV-1, pEPkan-S containing an I-SceI/KanR
443 selection cassette was used [52].

444 *Mammalian cell culture*

445 Mycoplasma-free spontaneously immortalised human keratinocyte (HaCaT) cells [72], HaCaT cells
446 stably expressing pUL21 (HaCaT21) [18], African green monkey kidney (Vero) cells (ATCC #CRL-
447 1586) and human embryonic kidney (HEK)293T cells (ATCC #CRL-3216) were maintained in
448 Dulbecco's Modified Eagle Medium with high glucose (Merck), supplemented with 10% (v/v) heat-
449 inactivated foetal calf serum (FCS) and 2 mM L-glutamine (complete DMEM) in a humidified 5% CO_2
450 atmosphere at 37°C. For protein purification, Freestyle 293F suspension cells (ThermoFisher) were
451 grown in Freestyle 293F medium (Gibco) on a shaking platform (125 rpm) in a humidified 8% CO_2
452 atmosphere at 37°C.

453 Doxycycline-inducible stably transfected Freestyle 293F cells expressing StrepII-$CERT_L$ and StrepII-
454 $CERT_L^{S132A}$ were generated using a piggyBac transposon-based system [68]. A 30 mL suspension
455 culture of Freestyle 293F cells at 1×10^6 cells/mL were transfected with a 5:1:1 mass ratio of PB-T-
456 $CERT_L^{(S132A)}$:PB-RN:PBase (35 µg total DNA) using Freestyle MAX transfection reagent (Invitrogen) as
457 per the manufacturer's instructions. After two days the cells were transferred to fresh media
458 supplemented with 500 µg/mL Geneticin (Gibco) and the drug selection was continued for two weeks
459 with media replenishment every three days.

460 *GFP affinity capture*

461 Monolayers of HEK293T cells grown in 9 cm dishes were transfected with TransIT-LT1 (Mirus) using
462 7.7 µg of pEGFP-N1 (for GFP alone), pUL21-GFP, or point mutants thereof, following the
463 manufacturer's instructions. At 24 hours post-transfection, the cells were harvested by scraping into the
464 medium, pelleted (220 g, 5 min, 4°C), washed three times with cold phosphate buffered saline (PBS)
465 and lysed at 4°C in 1 mL lysis buffer (10 mM Tris pH 7.5, 150 mM NaCl, 0.5 mM EDTA, 0.5% NP-40,
466 1:100 diluted EDTA-free protease inhibitor cocktail [Merck]) for 45 min before clarification (21,000×g,
467 10 min, 4°C). After immunoprecipitation with GFP-Trap beads (ChromoTek) performed in accordance
468 with the manufacturer's protocol, the samples were eluted by incubation at 95°C for 5 min in 45 µL 2×
469 SDS-PAGE loading buffer. Input and bound samples were separated by SDS-PAGE and analysed by
470 immunoblot.

471 *GST pulldown*

472 GST pulldown experiments were carried out in 96-well flat-bottomed plates (Greiner) using magnetic
473 glutathione beads (Thermo Scientific) to capture the GST-tagged pUL21 (bait protein). First, 0.5 nmol
474 of purified bait protein was incubated with the beads at 4°C for 30 min. The beads were washed three
475 times with wash buffer (20 mM Tris pH 8.5, 200 mM NaCl, 0.1% NP-40, 1 mM DTT, and 1 mM EDTA),
476 then incubated at 4°C for 60 min with various truncations of myc-CERT$_L$ (prey proteins), expressed
477 using the TNT SP6 High Yield Wheat Germ *in vitro* transcription/translation system (Promega) in
478 accordance with the manufacturer's protocol, followed by four washes in wash buffer. Protein was
479 eluted using wash buffer supplemented with 50 mM reduced glutathione before being analysed by SDS-
480 PAGE and immunoblotting.

481 *Antibodies*

482 The following antibodies with listed dilutions were used for immunoblotting: rabbit anti-CERT 1:10,000
483 (Abcam, ab72536), mouse anti-pUL21 1:50 [1F10-D12] [18] for Fig 1F [note: this monoclonal antibody
484 does not recognize pUL21^{V382E}], rabbit anti-pUL21 1:5000 [10] for Fig 5A and S3A, mouse anti-GAPDH
485 1:10,000 (GeneTex, GTX28245), mouse anti-Myc 1:4000 (Millipore, 05-724), mouse anti-PP1α 1:1000
486 (Santa Cruz, sc-271762), rabbit anti-pUL16 1:2000 [73], mouse anti-VP5 1:50 [DM165] [74], rabbit anti-
487 phospho-Akt substrates 1:1000 (Cell Signalling, 9611). Fluorescently labelled secondary antibodies
488 were used at 1:10,000 dilution: LI-COR IRDye 680T donkey anti-rabbit (926–68023) and goat anti-
489 mouse (926–68020), LI-COR IRDye 800CW conjugated donkey anti-rabbit (926–32213) and goat anti-
490 mouse (926–32210). For immunocytochemistry, mouse anti-pUL21 1:1 [L1E4-C10], which was
491 generated in the same immunisation experiments as anti-pUL21 [1F10-D12] [18], and Alexa Fluor 488
492 conjugated goat anti-mouse 1:1000 (Invitrogen, A21236) were used. For visualising HSV-1 plaques
493 mouse anti-gD (LP2) 1:50 [75] and HRP-conjugated rabbit anti-mouse 1:5000 (DaKo, P0161) were
494 used.

495 *Recombinant protein purification following bacterial expression*

496 All recombinant proteins were expressed in *Escherichia coli* T7 Express *lysY/I*^{q} cells (New England
497 Biolabs). Except for GST-PP1γ, cells were grown in 2×TY medium at 37°C to an OD_{600} of 0.8–1.2 before
498 cooling to 22°C and inducing protein expression by addition of 0.4 mM isopropyl β-D-
499 thiogalactopyranoside (IPTG). At 16–20 h post-induction, cells were harvested by centrifugation and
500 pellets were stored at -70°C until required. For GST-PP1γ, the 2×TY medium was supplemented with
501 1 mM $MnCl_2$ and the cultures were cooled to 18°C upon reaching an OD_{600} of 0.8, followed by induction
502 using 1 mM IPTG. For all recombinant proteins, cells were resuspended in lysis buffer (see below) at
503 4°C before lysis using a TS series cell disruptor (Constant Systems) at 24 kpsi. Lysates were cleared
504 by centrifugation (40,000×g, 30 min, 4°C) and incubated with the relevant affinity resins for 1 h at 4°C
505 before extensive washing (≥ 20 column volumes) and elution using the relevant elution buffer (see
506 below). Samples were concentrated and subjected to size exclusion chromatography (SEC, see below).
507 Fractions containing the desired protein as assessed by SDS-PAGE were pooled, concentrated, snap-
508 frozen in liquid nitrogen and stored at -70°C.

509 The lysis buffer for pUL21-GST (20 mM Tris pH 8.5, 300 mM NaCl, 0.5 mM $MgCl_2$, 1.4 mM β-
510 mercaptoethanol, 0.05% TWEEN-20) and GST-PP1γ (50 mM Tris pH 7.5, 500 mM NaCl, 1 mM $MnCl_2$,
511 0.5 mM $MgCl_2$, 1.4 mM β-mercaptoethanol, 0.05% TWEEN-20) was supplemented with 200–400 U
512 bovine DNase I (Merck) and 200 µL EDTA-free protease inhibitor cocktail (Merck). Cleared lysates were
513 incubated with glutathione Sepharose 4B (Cytiva), washed with wash buffer (20 mM Tris pH 8.5 [pUL21-
514 GST] or 7.5 [GST-PP1γ], 500 mM NaCl, 1 mM DTT, plus 1 mM $MnCl_2$ [GST-PP1γ only]) and the proteins
515 eluted using wash buffer supplemented with 25 mM reduced glutathione. SEC was performed using a
516 HiLoad Superdex S200 16/600 column (Cytiva) equilibrated in 20 mM Tris pH 8.5, 500 mM NaCl, 1 mM
517 DTT (pUL21-GST) or 50 mM Tris pH 7.5, 100 mM NaCl, 1 mM DTT (GST-PP1γ).

518 pUL21-H_6, pUL21^{V382E}-H_6 and H_6-pUL21C were purified in Tris buffer at pH 8.5 in with 500 mM NaCl
519 and H_6-miniCERT$_L$ was purified in Tris buffer at pH 7.5 with 150 mM NaCl. Lysis buffer (20 mM Tris, 20
520 mM imidazole, NaCl, 0.5 mM $MgCl_2$, 1.4 mM β-mercaptoethanol, 0.05% TWEEN-20) was
521 supplemented with 200–400 U bovine DNase I (Merck) and 200 µL EDTA-free protease inhibitor
522 cocktail (Merck). Cleared lysates were incubated with Ni-NTA agarose (Qiagen), washed with wash
523 buffer (20 mM Tris, 20 mM imidazole, NaCl) and eluted using elution buffer (20 mM Tris, 250 mM
524 imidazole, NaCl) SEC was performed using a HiLoad Superdex S200 column (Cytiva) equilibrated in
525 20 mM Tris, NaCl, 1 mM DTT.

526 *Recombinant protein purification following mammalian cell expression*

527 StrepII-CERT^{P} used for phosphatase assays was purified following transient transfection of Freestyle
528 293F cells, as described before [18]. StrepII-CERT$_L^{P}$ and StrepII-CERT$_L^{S132A}$ were purified from stably
529 transfected Freestyle 293F cells following induction with 2 µg/mL doxycycline (Fisher) for 72 hours.
530 Next, cells were harvested by centrifugation (220×g, 5 min, 4°C) and washed once with ice-cold PBS

before being resuspended in ice-cold lysis buffer with phosphatase inhibitors [StrepII-CERT$_L^P$ only] (100 mM Tris pH 8.0, 150 mM NaCl, 0.5 mM EDTA, 1 mM DTT, [10 mM tetrasodium pyrophosphate, 100 mM NaF, 17.5 mM β-glycerophosphate]). Cells were lysed by passage through a 23G needle six times and lysates were clarified by centrifugation (40,000 g, 30 min, 4°C). The supernatants were sonicated at 50% amplitude for 60 s using a sonicating probe (MSE) and the supernatants were passed through a 0.45 µm syringe filter (Sartorius). StrepII-tagged proteins were captured using 1 mL StrepTrap HP column (Cytiva) that had been pre-equilibrated in wash buffer (100 mM Tris pH 8.0, 150 mM NaCl, 0.5 mM EDTA, 1 mM DTT). After extensive washing (20 column volumes) the protein was eluted using wash buffer supplemented with 2.5 mM desthiobiotin. Pooled eluate was applied to a Superose 6 10/300 GL column (Cytiva) column equilibrated in ITC buffer (20 mM Tris pH 8.5, 500 mM NaCl, 0.5 mM Tris(2-carboxyethyl)phosphine [TCEP]) and fractions containing StrepII-CERT$_L$ as assessed by SDS-PAGE were pooled, concentrated and used for downstream applications.

Mutagenesis of viral genomes and generation of recombinant HSV-1

All HSV-1 strain KOS viruses used in this study were reconstituted from a bacterial artificial chromosome (BAC) [76] and the mutated strain was generated using the two-step Red recombination method [52] with the following primers:

Forward: 5′-CGGCTCGTAGGCCGGTACACACAGCGCCACGGCCTGTACG**AA**CCTCGGCCCGACG ACCCAGTAGGATGACGACGATAAGTAGGG

Reverse: 5′-CGTTGATGGCATCGGCCAAGACTGGGTCGTCGGGCCGAGG**TT**CGTACAGGCCGTG GCGCTGTCAACCAATTAACCAATTCTGATTAG

The generation of pUL21 deletion mutant (ΔpUL21) was described previously [18]. To generate the P0 stocks, Vero cells were transfected with the recombinant BAC DNA together with pGS403 encoding Cre recombinase (to excise the BAC cassette) using TransIt-LT1 (Mirus) following the manufacturer's instructions. After 3 days the cells were scraped into the media, sonicated at 50% power for 30 s in a cup-horn sonicator (Branson), and titrated on Vero cell monolayers. The subsequent stocks were generated by infecting either Vero (HSV-1 WT) or HaCaT pUL21 cells (HSV-1 mutants) at MOI of 0.01 for 3 days. The cells were then scraped and isolated by centrifugation at 1,000×g for 5 min. Pellets were resuspended in 1 mL of complete DMEM supplemented with 100 U/mL penicillin, 100 µg/mL streptomycin and freeze/thawed thrice at -70°C before being aliquoted, titered on Vero cell monolayers, and stored at -70°C until required. The presence of the desired mutation in the reconstituted virus genomes was confirmed by sequencing the pUL21 gene.

Metabolic labelling and lipid extraction for thin layer chromatography

Metabolic labelling was performed using sub-confluent (60–80% confluence) HaCaT or HaCaT21 cells grown in a 6-well plate. For analysis of stable cell lines, the cells were pre-treated for 30 min with complete DMEM containing 1 µM N-(3-Hydroxy-1-hydroxymethyl-3-phenylpropyl)dodecanamide (HPA-

566 12, Tokyo Chemical Industry) dissolved in 0.1% dimethyl sulfoxide (DMSO, Merck), or 0.1% DMSO
567 alone, and HPA-12 or DMSO were retained at the same concentrations throughout the subsequent
568 incubation steps. For infection, cells were infected (below) 14 hours before metabolic labelling.

569 For metabolic labelling, wells were washed twice with warm PBS before incubation in 500 µL pre-
570 warmed DMEM with 1% (v/v) Nutridoma (Merck) supplemented with 5 µM clickable sphingosine
571 (Cayman Chemical) for 5 min (pulse). Next, cells were washed twice with warm PBS and 1 mL of pre-
572 warmed DMEM with 1% (v/v) Nutridoma was added to each well, followed by incubation at 37°C for the
573 indicated times of chase. Click-Sph was stored as a 3.3 mM ethanolic stock solution at -20°C.

574 At the indicated times of chase, the plate with cells was transferred onto the ice, washed twice with 1
575 mL ice-cold PBS, scraped into 300 µL of ice-cold PBS and transferred into appropriate 1.5 mL
576 microcentrifuge tubes containing 600 µL of methanol. To each tube 150 µL of chloroform was added,
577 followed by vigorous vortexing. The precipitated protein was pelleted (20,000×g, 1 min) at room
578 temperature (RT). The organic supernatant was transferred to separate 2 mL tubes containing 300 µL
579 chloroform. 600 µL of 0.1% acetic acid in H_2O was subsequently added to each tube to induce formation
580 of two phases. Following extensive vortexing, the phases were separated by centrifugation (20,000×g,
581 1 min, RT) and the lower phase was transferred to a new 1.5 mL microcentrifuge tube. This lipid-
582 containing solvent phase was dried in a UniVapo centrifugal vacuum concentrator (UniEquip) at 30°C
583 for 20 min.

584 If required for SDS-PAGE analysis, the protein pellet was solubilized with 5 µL 10% (w/v) SDS, diluted
585 in 75 µL lysis buffer (20 mM Tris 7.5, 150 mM NaCl, 1% (v/v) Triton X-100), boiled for 10 min and
586 sonicated at 75% power for 60 s in a cup-horn sonicator (Branson). The protein samples were mixed
587 with 5× loading buffer before being subjected to SDS-PAGE analysis.

588 *Click reaction and thin layer chromatography of labelled lipids*

589 Lipid standards (16:0(Alkyne)-18:1 PC [Avanti], pacFA GalCer [Avanti], d18:1(Alkyne)-6:0 Cer [Cayman
590 Chemicals], 18:0(Alkyne) Sph [Cayman Chemicals]) or extracted lipids (above) were resuspended in
591 20 µL of 1:1 chloroform:ethanol. To each tube 1 µL of Tris((1-benzyl-4-triazolyl)methyl)amine (TBTA)
592 solution (2.5 mM in DMSO; Merck), 10 µL of Tetrakis(acetonitrile)copper(I) tetrafluoroborate (10 mM in
593 acetonitrile; Merck) and 1 µL of 3-azido-7-hydroxycoumarin solution (1 mM in EtOH; Jena Bioscience)
594 was added. After brief mixing, the reaction was dried in a UniVapo centrifugal vacuum concentrator
595 (UniEquip) for 10 min at 45°C. Lipids were dissolved in 20 µL of 65:25:4:1
596 chloroform:methanol:water:acetic acid, of which 8 µL was spotted on a 20×10 cm HPTLC Silica gel 60
597 plates (Merck). When dried, the plate was developed for 5 cm with 65:25:4:1
598 chloroform:methanol:water:acetic acid, dried again and developed for 9 cm with 1:1
599 hexane:ethylacetate. Labelled lipids were visualized via UV illumination using a G:BOX Chemi XX9
600 (Syngene), bands were quantified using the Image Studio Lite software (LI-COR) with local background
601 subtraction, and statistical tests were performed using Prism 7 (GraphPad Software).

602 *Virus infections*

603 Monolayers of indicated cells were infected by overlaying with the appropriate viruses, diluted in
604 complete DMEM to the specified MOI. The time of addition was designated 0 hours post-infection (hpi).
605 Cells were incubated with the inoculum at 37°C in a humidified 5% CO_2 atmosphere for 1 hour, rocking
606 the tissue culture plate housing the monolayers every 15 min, before complete DMEM supplemented
607 with 100 U/mL penicillin, 100 µg/mL streptomycin was added to dilute the original infection medium five-
608 fold. Infected cells were incubated at 37°C in a humidified 5% CO_2 atmosphere and harvested at the
609 specified times.

610 *Immunoblotting*

611 For analysis of protein expression and phosphorylation, cells were washed two times with ice-cold 50
612 mM Tris pH 8.5, 150 mM NaCl and scraped into 100 µL of ice-cold lysis buffer (50 mM Tris pH 8.5,
613 150mM NaCl, 1% (v/v) Triton-X100, 1% (v/v) EDTA-free protease inhibitor cocktail [Merck], 10 mM
614 tetrasodium pyrophosphate, 100 mM NaF and 17.5 mM β-glycerophosphate). After 30 min incubation
615 on ice, the lysates were sonicated (two 15 s pulses at 50% power) in a cup-horn sonicator (Branson)
616 followed by centrifugation at 20,000×g for 10 min. For all samples, protein concentrations were
617 determined using a BCA assay (Peirce) and normalized protein lysates were analysed by SDS-PAGE.
618 For enhanced separation of phosphorylated proteins, 7% (w/v) acrylamide gels contained 50 µM $MnCl_2$
619 and 25 µM PhosTag reagent (Wako) where indicated. Separated proteins were then transferred to
620 nitrocellulose membranes using the Mini-PROTEAN system (Bio-Rad) and analysed by
621 immunoblotting, signals being detected using Odyssey CLx Imaging System (LI-COR). For quantitation
622 of CERT phosphoform relative abundance, the signal for $CERT^{O}$ band alone and for all CERT bands
623 ($CERT^{O}$ + $CERT^{P}$) were quantitated using Image Studio Lite software (LI-COR) with local background
624 subtraction. Statistical tests were performed using Prism 7 (GraphPad Software).

625 *Analytical SEC of miniCERT$_L$:pUL21C complex*

626 Analytical SEC experiments were performed using Superdex 200 10/300 GL (Cytiva) column
627 equilibrated in 20 mM Tris pH 8.5, 500 mM NaCl, 1 mM DTT. To allow complex formation, 200 µL of
628 140 µM H_6-miniCERT$_L$ and 680 µL of 55.4 µM H_6-pUL21C were mixed and incubated for 15 min at room
629 temperature prior to injection.

630 *Isothermal titration calorimetry (ITC)*

631 ITC experiments were performed at 25°C using an MicroCal PEAQ-ITC automated calorimeter (Malvern
632 Panalytical). Proteins were transferred into ITC buffer (20 mM Tris pH 8.5, 500 mM NaCl, 0.5 mM TCEP)
633 either by SEC or extensive dialysis prior to experiments. Titrants (StrepII-CERT$_L^{P}$ at 192–328 µM,
634 StrepII-CERT$_L^{S132A}$ at 196–334 µM or H_6-miniCERT$_L$ at 195–376 µM) were titrated into titrates (pUL21-
635 H_6 at 20–33 µM, pUL21^{V382E}-H_6 at 19.5–32 µM or H_6-pUL21C at 30–32.5 µM) using either 19×2 µL or

636 12×3 µL injections. Data were analysed using the MicroCal PEAQ-ITC analysis software (Malvern
637 Panalytical) and fitted using a one-site binding model.

638 *Multi-angle light scattering (MALS)*

639 MALS data were collected immediately following SEC (SEC-MALS) by inline measurement of static
640 light scattering (DAWN 8+; Wyatt Technology), differential refractive index (Optilab T-rEX; Wyatt
641 Technology), and UV absorbance (1260 UV; Agilent Technologies). Samples (100 µL) were injected
642 onto an Superose 6 increase 10/300 GL column (Cytiva) equilibrated in in 20 mM Tris pH 8.5, 500 mM
643 NaCl, 0.5 mM TCEP at 0.4 mL/min. The protein samples were injected at the concentration of 2 mg/mL.
644 Molecular masses were calculated using ASTRA 6 (Wyatt Technology) using a protein dn/dc of
645 0.186 mL/g.

646 *Small-angle X-ray scattering (SAXS)*

647 SAXS experiments were performed in batch mode (H_6-pUL21C and H_6-miniCERT$_L$) or inline following
648 SEC (H_6-pUL21C:H_6-miniCERT$_L$) at EMBL-P12 bioSAXS beam line (PETRAIII, DESY, Hamburg,
649 Germany) [77,78].

650 For SAXS in batch mode, scattering data ($I(s)$ versus s, where $s = 4\pi\sin\theta/\lambda$ nm^{-1}, 2θ is the scattering
651 angle, and λ is the X-ray wavelength, 0.124 nm) were collected from the indicated batch samples and
652 a corresponding solvent blank (20 mM Tris pH 8.5, 500 mM NaCl, 3% (v/v) glycerol, 1 mM DTT). The
653 scattering profiles of H_6-miniCERT$_L$ (1.73, 2.59, 3.46 and 6.91 mg/mL) and H_6-pUL21C (0.76 mg/mL)
654 were measured in continuous-flow mode using an automated sample changer (30 µL sample at 20°C;
655 1 mm pathlength). The sample and buffer measurements were measured as 100 ms data frames on a
656 Pilatus 6M area detector for total exposure times of 2.1 and 2.6 s, respectively. For H_6-miniCERT$_L$, the
657 resulting SAXS curves were extrapolated to infinite dilution.

658 For SEC-SAXS experiments, the scattering data were recorded using a Pilatus 6M detector (Dectris)
659 with 1 s sample exposure times for a total of 3600 data frames spanning the entire course of the SEC
660 separation. Proteins were mixed at 1:1 molar ratio, incubated on ice for 15 min, and then concentrated
661 using a centrifugal concentrator to the desired concentration as estimated from absorbance using
662 extinction coefficients [79] calculated assuming a 1:1 molar ratio. 40 µL of purified H_6-pUL21C:H_6-
663 miniCERT$_L$ (4.3 mg/mL) was injected at 0.35 mL/min onto an Superdex 200 Increase 5/150 GL column
664 (Cytiva) equilibrated in 20 mM Tris pH 8.5, 500 mM NaCl, 3% (v/v) glycerol, 1 mM DTT. SAXS data
665 were recorded from a single peak (frames 1245–1296 s) and solvent blank was collected from pre-
666 elution frames (frames 247–411). Primary data reduction was carried out using CHROMIXS [80] and
667 2D-to-1D radial averaging was performed using the SASFLOW pipeline [81]. Processing and analysis
668 of the SAXS output was performed using the ATSAS 3.0.2 software package [82]. The extrapolated
669 forward scattering intensity at zero angle, $I(0)$, and the radius of gyration, R_g, were calculated from the
670 Guinier approximation ($\ln I(s)$ vs s^2, for $sR_g < 1.3$). The maximum particle dimension, D_{max}, was estimated

671 based on the probable distribution of real-space distances *p*(*r*) which was calculated using GNOM [83].
672 A concentration-independent estimate of molecular weight was determined using a Bayesian
673 consensus method [84]. All structural parameters are reported in Table S1.

674 *Ab initio* modelling was performed using GASBOR [49] and figures show the models that best fit their
675 corresponding SAXS profiles (lowest χ^2). Pseudo-atomic modelling was performed using CORAL [85].
676 For H_6-miniCERT$_L$, crystal structures of the CERT PH (PDB ID 4HHV) [24] and START (PDB ID 2E3M)
677 [25] domains were used, the latter including predicted secondary structure as modelled by I-TASSER
678 [86] for intron 11 (residues 371-396), present only in CERT$_L$. The miniCERT$_L$ 23 amino acid linker and
679 the purification tag (MAH_6) were modelled using CORAL. The model with the best fit was superimposed
680 onto the PH:START crystal structure (PDB ID 5JJD) [46] by aligning the START domains using PyMOL
681 version 2.5.2 (Schrödinger). For H_6-pUL21C, the N-terminal (MAH_6QD) and C-terminal (HGQSV)
682 elements missing from the crystal structure (PDB ID 5ED7) [50] were modelled using CORAL. For H_6-
683 pUL21C:H_6-miniCERT$_L$, the heterodimer was modelled using the SAXS curve of the complex using a
684 fixed conformation of H_6-pUL21C and mobile CERT domains, with unstructured elements modelled as
685 above. All the models were assessed for fit to the corresponding SAXS profiles (χ^2 and CorMap) using
686 CRYSOL [87].

687 *Differential scanning fluorimetry*

688 Differential scanning fluorimetry experiments were carried out using Viia7 real-time PCR system
689 (Applied Biosystems) and 1× Protein Thermal Shift dye (Applied Biosystems). The assay buffer (20 mM
690 Tris pH 8.5, 500 mM NaCl, 1 mM DTT) was mixed with dye stock solution and protein solution (H_6-
691 pUL21 or H_6-pUL21^{V382E} in an 8:1:1 ratio, giving 1 ng protein in a final volume of 20 µL, and
692 measurements were performed in triplicate. Samples were heated from 25 to 95°C at 1 degree per 20 s
693 and fluorescence was monitored at each increment. The melting temperature (T_m) is the inflection point
694 of the sigmoidal melting curve, determined by non-linear curve fitting to the Boltzmann equation using
695 Prism 7 (GraphPad Software).

696 In vitro *dephosphorylation assays*

697 Dephosphorylation assays were performed upon 0.5 µM of purified CERT^P using a fixed concentration
698 of GST-PP1γ (25 nM) in the presence of pUL21-H_6 or pUL21^{V382E} -H_6 at the indicated concentrations.
699 Reactions (50 µL) proceeded in assay buffer (150 mM NaCl, 20 mM Tris pH 8.5, 0.1% TWEEN-20, 1
700 mM $MnCl_2$) for 30 min at 30°C before being stopped by the addition of 50 µL of 2× SDS-PAGE loading
701 buffer and boiling at 95°C for 5 min. Samples were analysed by SDS-PAGE using 7% (w/v) acrylamide
702 gels supplemented with 25 µM PhosTag reagent and 50 µM $MnCl_2$ and the protein was visualized using
703 InstantBlue Coomassie stain (Expedeon). To measure the ratio of CERT^O to total CERT, Coomassie-
704 stained gels were scanned using an Odyssey CLx Imaging System (LI-COR). The signals detected in
705 the 700 nm channel for the CERT^O band alone and for all CERT bands (CERT^O + CERT^P) were
706 quantitated using Image Studio Lite software (LI-COR) with local background subtraction.

707 *Plaque size analysis*

708 Confluent monolayers of Vero or HaCaT cells in 6-well tissue culture plates were infected with 100
709 plaque forming units of the indicated virus diluted in complete DMEM to a final volume of 500 µL.
710 Following the adsorption for 1 h at 37°C in a humidified 5% CO_2 atmosphere, rocking the plate every
711 15 min, the cells were overlaid with plaque assay media (DMEM supplemented with 0.3% high viscosity
712 carboxymethyl cellulose, 0.3% low viscosity carboxymethyl cellulose, 2% (v/v) FCS, 2 mM L-glutamine,
713 100 U/mL penicillin and 100 µg/mL streptomycin) and incubated for further 48 hours. Next, cells were
714 fixed with 3.7% (v/v) formal saline for 20 min, washed three times with PBS and incubated for 1 h with
715 mouse anti-gD (LP2) [75], diluted 1:50 in blocking buffer (PBS supplemented with 1% (w/v) BSA and
716 0.1% TWEEN-20). Cells were washed thrice in PBS and incubated for 30 min with HRP-conjugated
717 rabbit anti-mouse antibody (DaKo, P0161) diluted 1:5000 in blocking buffer, followed by two subsequent
718 PBS washes and one wash with ultrapure water. Plaques were visualized using the TrueBlue
719 peroxidase substrate in accordance with the manufacturer's instructions (Seracare). Plaques were
720 scanned at 1200 dpi and plaque areas were measured using Fiji [88,89].

721 *Single-step (high MOI) virus growth assays*

722 Virus growth assays were performed in technical duplicate for each independent experiment.
723 Monolayers of HaCaT or Vero cells were infected with the indicated viruses diluted in complete DMEM
724 to an MOI of 10. The time of virus addition was designated 0 hpi. After adsorption for 1 h at 37°C in a
725 humidified 5% CO_2 atmosphere, rocking the plates every 15 min, extracellular virus particles were
726 neutralized with an acid wash (40 mM citric acid, 135 mM NaCl, 10 mM KCl, pH 3.0) for 1 min and cells
727 were then washed three times with PBS before being subsequently overlaid with complete DMEM. At
728 designated times post-infection, cells were harvested by freezing the plate at -70°C. When all plates
729 were frozen, samples were freeze/thawed one more time before scraping and transferring to 1.5 mL
730 tubes and storing at -70°C until titration. Titrations were performed on monolayers of Vero cells. Serial
731 dilutions of the samples were used to inoculate the cells for 1 h, followed by overlaying with DMEM
732 containing 0.3% high viscosity carboxymethyl cellulose, 0.3% low viscosity carboxymethyl cellulose,
733 2% (v/v) FBS, 2 mM L-glutamine, 100 U/mL penicillin and 100 µg/mL streptomycin. Three days later,
734 cells were fixed in 3.7% (v/v) formal saline for 20 min, washed with water and stained with 0.1% toluidine
735 blue. Statistical tests were performed using Prism 7 (GraphPad Software).

736 *Virus release assays*

737 Monolayers of HaCaT or Vero cells were infected as described above for single-step virus growth
738 assays, infections being performed in technical duplicate or triplicate for each independent experiment.
739 At 12 hpi, the media (500 µL) were harvested to 1.5 mL Eppendorf tubes, spun down for 5 min at 1000
740 g to remove any detached cells, 300 µL of the supernatant was carefully transferred to fresh tubes and
741 stored at -70°C until titration. The cells were overlaid with 500 µL of fresh DMEM and the plates were

742 immediately frozen at -70°C. Titrations were performed on monolayers of Vero cells as described
743 above. Statistical tests were performed using Prism 7 (GraphPad Software).

744 *Immunocytochemistry*

745 Cells grown on #1.5 coverslips were infected at an MOI of 1 as described above. At 14 hpi, cells were
746 washed with PBS and incubated with freezing cold (-20°C) methanol for 5 min at -20°C. Coverslips
747 were washed with PBS, followed by incubation with blocking buffer (1% (w/v) BSA in PBS) for 30 min
748 at RT. Primary antibodies (above) were diluted in blocking buffer and incubated with coverslips for 1 h.
749 Coverslips were washed ten times with PBS before incubation for 45 min with the secondary antibodies
750 (above) diluted in blocking buffer. Coverslips were washed ten times in PBS and ten times in ultrapure
751 water before mounting on slides using Mowiol 4–88 (Merck) containing 200 nM 4′,6-diamidino-2-
752 phenylindole (DAPI). Images were acquired using an inverted Olympus IX81 widefield microscope with
753 a 60× Plan Apochromat N oil objective (numerical aperture 1.42) (Olympus) and Retiga EXi Fast1394
754 interline CCD camera (QImaging).

755 **Acknowledgements**

756 The synchrotron SAXS data was collected at beamline P12 operated by EMBL Hamburg at the PETRA
757 III storage ring (DESY, Hamburg, Germany). We thank Chris Boutell (MRC-University of Glasgow
758 Centre for Virus Research), John Willis (University of Pennsylvania) and David Ron (Cambridge
759 Institute for Medical Research) for kindly providing antibodies or plasmids. This work was funded by a
760 Royal Society University Research Fellowship (UF100371), a Royal Society Enhancement Award
761 (RGF\EA\180151) and a Wellcome Trust Senior Research Fellowship (219447/Z/19/Z) to JED, a
762 Biotechnology and Biological Sciences Research Council (BBSRC) Research Grant (BB/M021424/1)
763 and a Medical Research Council Research Grant (MR/T016493/1) to CMC, and by a Sir Henry Dale
764 Fellowship, jointly funded by the Wellcome Trust and the Royal Society (098406/Z/12/B) to SCG. DIS
765 and CMJ acknowledge the support of iNEXT-Discovery (project number 871037) funded by the Horizon
766 2020 programme of the European Commission. The funders had no role in study design, data collection
767 and analysis, decision to publish, or preparation of the manuscript. For the purpose of open access, the
768 authors have applied a Creative Commons Attribution (CC BY) licence to any Author Accepted
769 Manuscript version arising from this submission.

770 **Data availability**

771 The SAXS data measured for each concentration, with an accompanying report, are available in the
772 Small Angle Scattering Biological Data Bank (SASBDB) [90], entries SASDNB7, SASDNC7 and
773 SASDND7.

774 **Conflict of Interest**

775 The authors declare they have no conflict of interest.

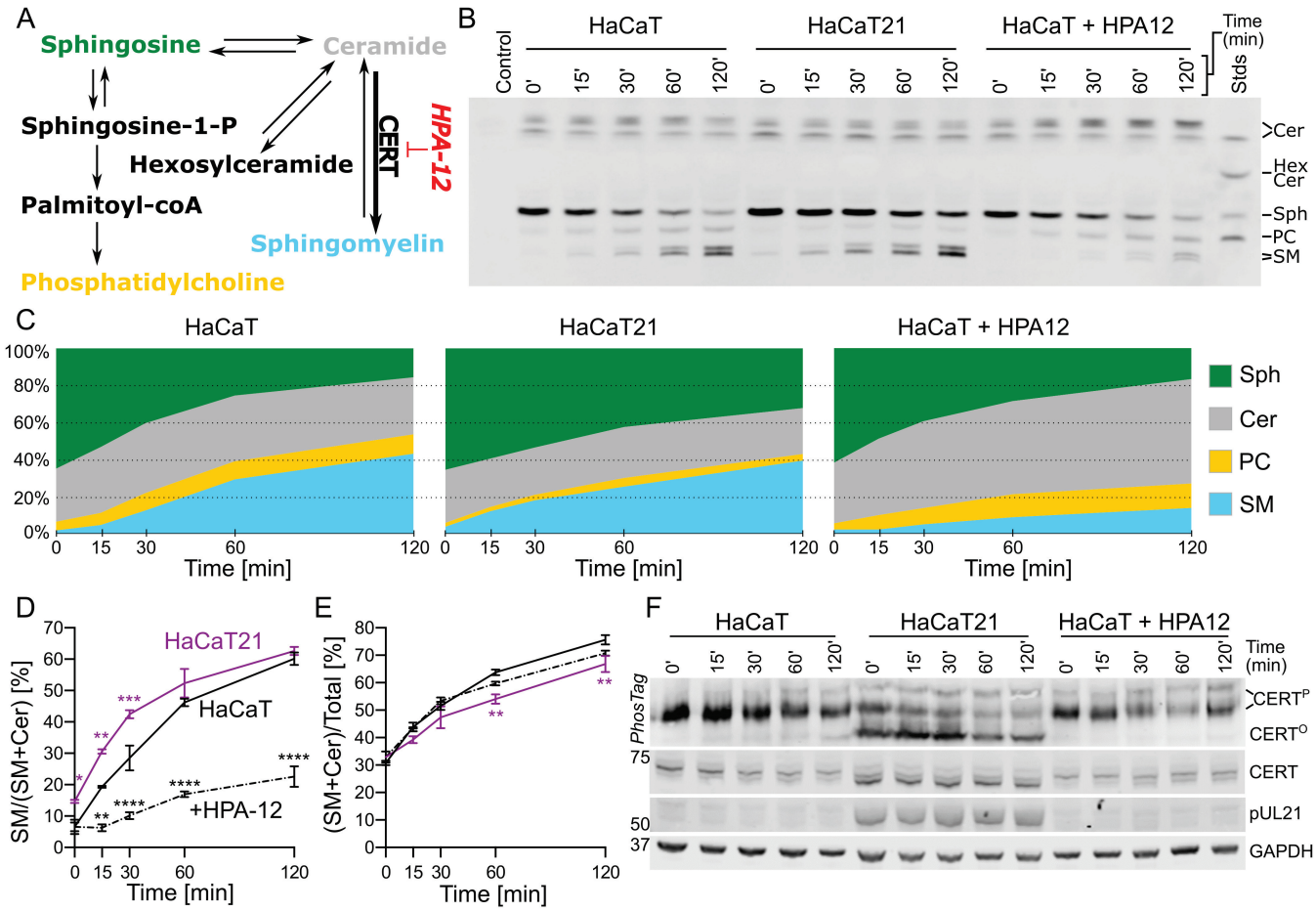

Figure 1. HSV-1 pUL21 alters the rate of ceramide to sphingomyelin conversion in cultured cells. (**A**) Simplified schematic diagram of sphingolipid biosynthetic pathways that lead from sphingosine (Sph) to sphingomyelin (SM) and glycosphingolipids (hexosylceramide; HexCer), or to phosphatidylcholine (PC) via a "salvage" pathway. Ceramide (Cer) to SM conversion is accelerated by the transport protein CERT, which is selectively inhibited by HPA-12. (**B**) Rate of Sph conversion to Cer, SM or PC was measured in HaCaT cells, untreated or treated with 1 μM HPA-12, and in HaCaT cells stably expressing pUL21 (HaCaT21). Cells were incubated with 5 μM 'clickable' alkyne-Sph (pulse) for 5 min and harvested for lipid extraction either immediately (0 min) or at the indicated times (chase). Extracted lipids were bioconjugated to 3-azido-7-hydroxycoumarin, separated by HPTLC and detected using UV light. Separated lipids were identified using clickable standards (Stds) and previous literature [42]. Data is from one representative experiment of two independent repeats. (**C**) Quantitation of the lipid intensities from (**B**) as determined by densitometry and represented as percentage fraction of total signal. (**D**) Rate of SM synthesis expressed as its fraction in the cumulative signal for SM and Cer. (**E**) The ratio of alkyne-Sph incorporated into either Cer or SM as a proportion of total alkyne-lipid signal, representing the influx of Sph into the SM biosynthetic pathway. For (**D**) and (**E**) the data represents two independent experiments (mean ± SEM). Data points are labelled if significantly different to parental HaCaT cells: **, $p < 0.01$; ***, $p < 0.001$; ****, $p < 0.0001$ (two-way ANOVA with Dunnett's multiple comparisons test). (**F**) The re-solubilised proteins precipitated during lipid extraction were analysed by SDS-PAGE and immunoblotting using the antibodies listed. Where indicated, the gel was supplemented with PhosTag reagent to retard the migration of phosphorylated proteins, thus enhancing

796 the separation of CERT that is hypo- ($CERT^{O}$) or hyper-phosphorylated ($CERT^{P}$). GAPDH serves as a
797 loading control.

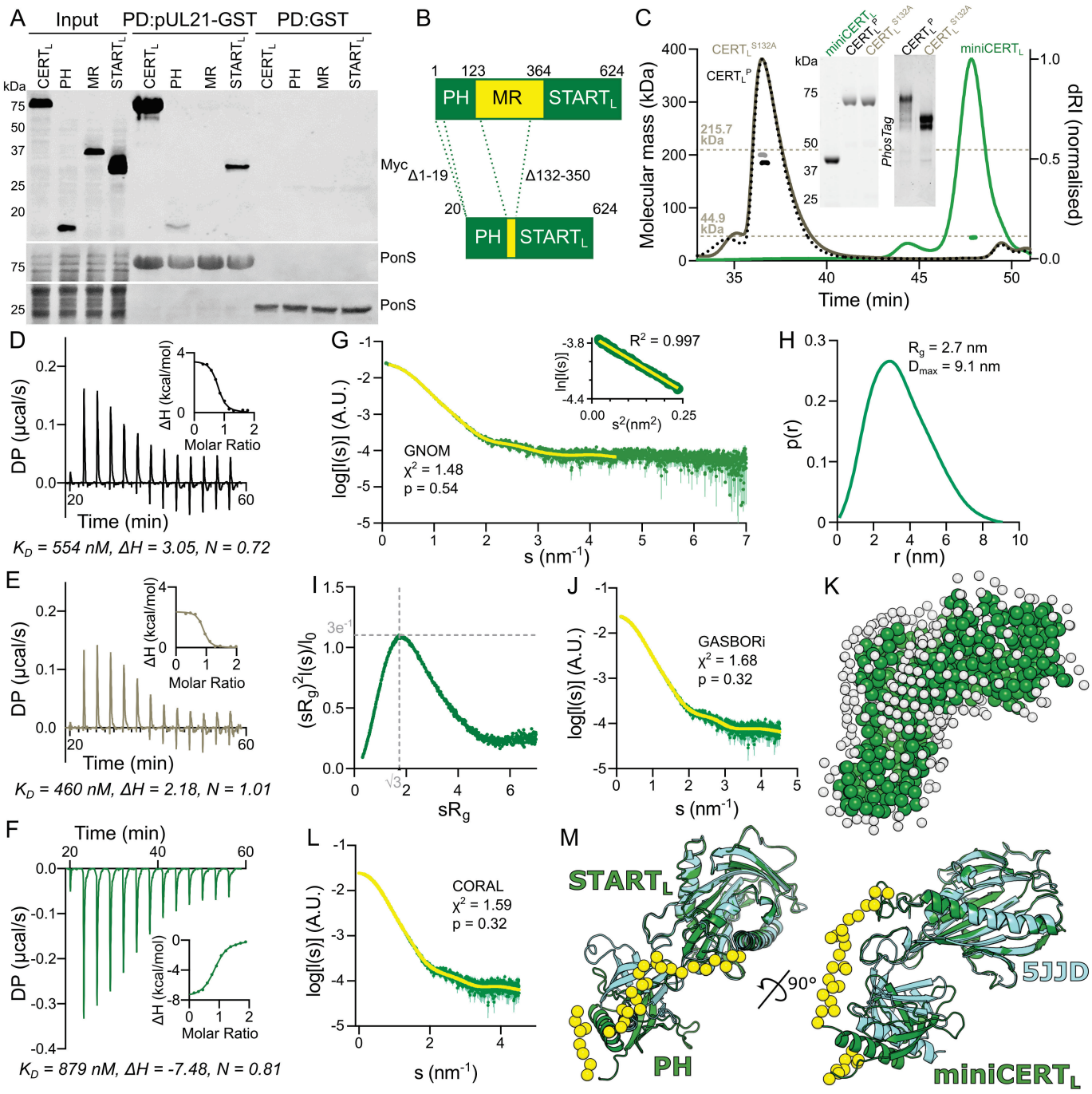

Figure 2. pUL21 binds to the PH and START$_L$ domains of CERT$_L$, and to a monomeric form of CERT$_L$ comprising just the PH and START$_L$ domains (miniCERT$_L$). (**A**) Minimal binding elements of CERT$_L$ were determined via pull down (PD) experiment using immobilised purified pUL21-GST or GST alone to capture myc-tagged full-length CERT$_L$ or truncations thereof expressed via *in vitro* transcription/translation. Captured proteins were subjected to SDS-PAGE and immunoblotting using an anti-myc antibody. Ponceau S (PonS) staining of the immunoblot membrane before blocking shows equal and efficient capture of the bait proteins across the tested conditions. (**B**) Schematic representation of miniCERT$_L$. Dotted lines indicate the regions of full-length CERT$_L$ that were omitted. (**C**) SEC-MALS elution profiles (normalized differential refractive index, dRI) of StrepII-CERT$_L$ (black dotted), StrepII-CERT$_L^{S132A}$ (grey solid) and H$_6$-miniCERT$_L$ (green solid). Weight-averaged molecular

808 masses (coloured solid lines) are shown across the elution peaks. The expected molecular masses for
809 trimeric StrepII-CERT$_L$ and StrepII-CERT$_L^{S132A}$, and for monomeric H$_6$-miniCERT$_L$, are shown as dotted
810 horizontal lines. Inset shows Coomassie-stained SDS-PAGE of the samples used for SEC-MALS (left),
811 plus SDS-PAGE supplemented with PhosTag reagent (right) of the StrepII-CERT$_L$ proteins. (**D–F**)
812 Representative ITC titration curve of pUL21-H$_6$ binding to (**D**) StrepII-CERT$_L$, (**E**) StrepII-CERT$_L^{S132A}$,
813 and (**F**) H$_6$-miniCERT$_L$. DP, differential power. Insets show normalized binding curves with integrated
814 changes in enthalpy (ΔH) as a function of molar ratio. The affinity (K_D), ΔH and stoichiometry (N) for the
815 presented titrations are displayed below. (**G**) SAXS profile measured for H$_6$-miniCERT$_L$. The reciprocal-
816 space fit of the $p(r)$ profile to the SAXS data is shown as a yellow line. χ2, fit quality; p, Correlation Map
817 (CorMap) probability of systematic deviations between the model fit and the scattering data [81]. Inset
818 shows the Guinier plot (sR_g < 1.3), which is linear as expected for an aggregate- and repulsion-free
819 system. (**H**) The real-space distance distribution function, $p(r)$, calculated from the SAXS profile. (**I**)
820 Dimensionless Kratky plot of the SAXS data. Grey dotted lines indicate the expected maximum of the
821 plot for a compact protein ($sR_g = \sqrt{3}$, $(sR_g)^2 I(s)/I(0) = 3e^{-1}$) [91]. (**J**) Fit of an *ab initio* dummy-residue
822 model calculated using GASBOR to the SAXS profile, and (**K**) representative GASBOR dummy-residue
823 model. White spheres indicate modelled water beads of the hydration shell. (**L**) Fit to the SAXS profile
824 of the pseudo-atomic model of H$_6$-miniCERT$_L$ obtained using CORAL. (**M**) CORAL pseudo-atomic
825 model of H$_6$-miniCERT$_L$ (green ribbons) superimposed onto the crystal structure of the complex
826 between the CERT PH and START domains (PDB ID 5JJD; cyan ribbons) [46] by aligning the
827 START/START$_L$ domains. Superposition is shown in orthogonal orientations where the linker regions
828 or termini that were modelled by CORAL are depicted as yellow spheres.

829

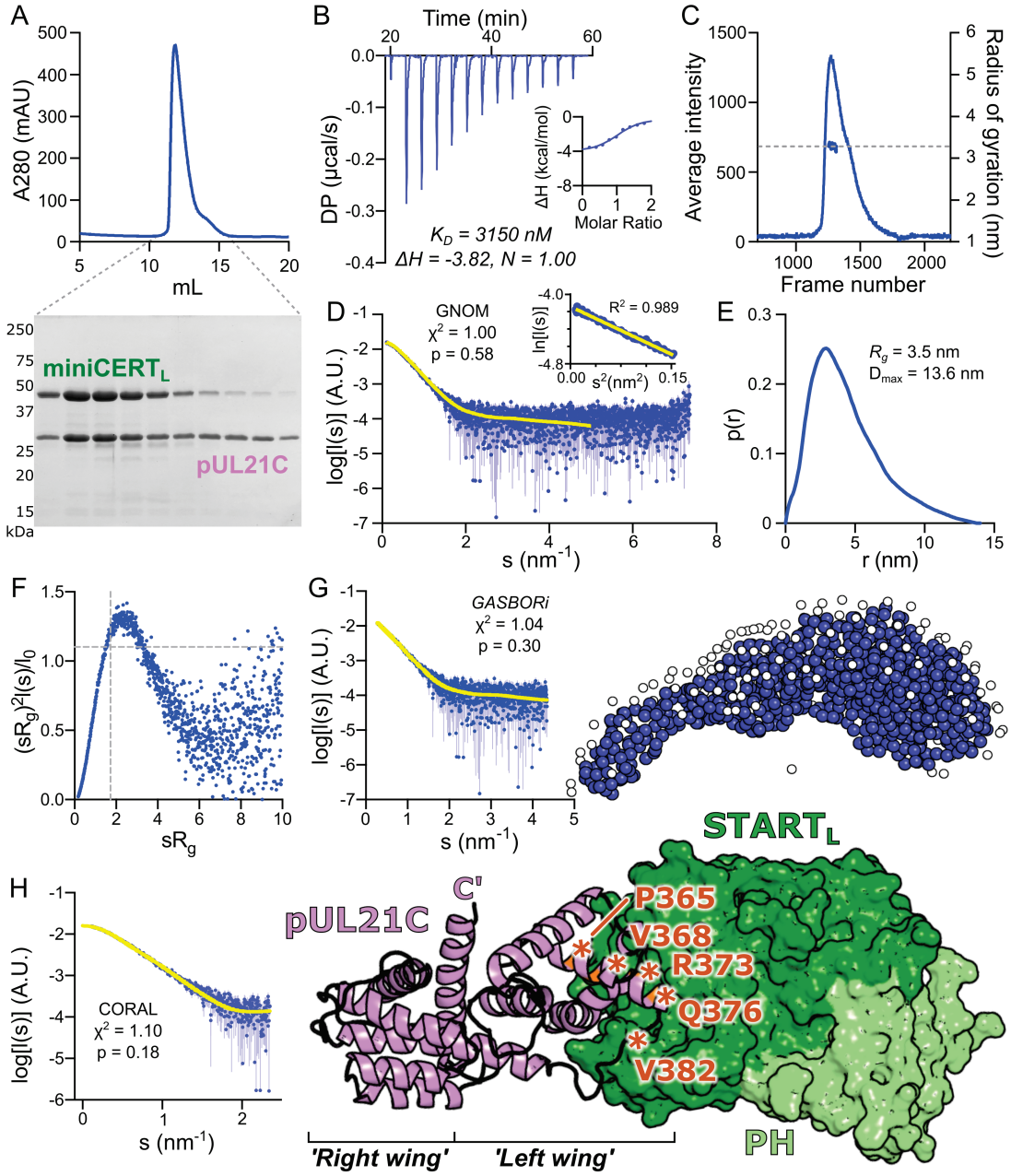

Figure 3. Solution structure of the H$_6$-pUL21C:H$_6$-miniCERT$_L$ heterodimer. (**A**) SEC elution profile (A_{280}) of the H$_6$-pUL21C:H$_6$-miniCERT$_L$ complex, pre-formed in the presence of 1.32-fold molar excess of H$_6$-pUL21C. Dotted lines indicate fractions that were collected and subjected to SDS-PAGE analysis with Coomassie staining, revealing co-elution of the two proteins. (**B**) Representative ITC titration curve of H$_6$-pUL21C binding to H$_6$-miniCERT$_L$. DP, differential power. Inset shows normalized binding curve with integrated changes in enthalpy (ΔH) as a function of molar ratio. The ranges of the vertical axes are identical to Fig 2F. The affinity (K_D), ΔH and stoichiometry (N) for the presented titration are displayed below. (**C**) SEC elution profile (partial integrated scattered X-ray intensity vs. data frame number) obtained during SEC-SAXS analysis of H$_6$-pUL21C:H$_6$-miniCERT$_L$ complex. Dashed line indicates the calculated radius of gyration (R_g) across the frames averaged for structural analyses. (**D**) Averaged SAXS profile of the H$_6$-pUL21C:H$_6$-miniCERT$_L$ complex. The reciprocal-space fit of the $p(r)$ profile to the SAXS data is shown as a yellow line. χ^2, fit quality; p, Correlation Map (CorMap) probability

842 of systematic deviations between the model fit and the scattering data [81]. Inset displays the Guinier
843 plot (sR_g < 1.3), which is linear as expected for an aggregate- and repulsion-free system. (**E**) Real-
844 space distance distribution function, $p(r)$, calculated from the SAXS profile. (**F**) Dimensionless Kratky
845 plot of the SAXS data. Grey dotted lines indicate the expected maximum of the plot for a compact
846 protein ($sR_g = \sqrt{3}$, $(sR_g)^2 I(s)/I(0) = 3e^{-1}$). (**G**) *Ab initio* modelling of H_6-miniCERT$_L$:H_6-pUL21C using
847 GASBOR. Fit of the calculated scattering (yellow) to the SAXS profile is shown, as is a representative
848 dummy-residue model (blue spheres) with modelled water beads of the hydration shell (white spheres).
849 (**H**) Pseudo-atomic model of the H_6-miniCERT$_L$:H_6-pUL21C complex generated using CORAL. The fit
850 of the computed scattering (yellow) to the SAXS profile is shown. pUL21C is shown as a violet ribbon
851 with C terminus labelled and miniCERT$_L$ as a green molecular surface (PH, light green; START$_L$, dark
852 green). The left and right 'wings' of the dragonfly-like pUL21C fold [50] are labelled. For clarity, regions
853 absent from the crystal structures that were modelled by CORAL are not displayed. Orange asterisks
854 indicate pUL21C residues at the interface with miniCERT$_L$ that were selected for further investigation.
855 Additional pseudo-atomic models that also fit the scattering data are shown in Fig S3.

856

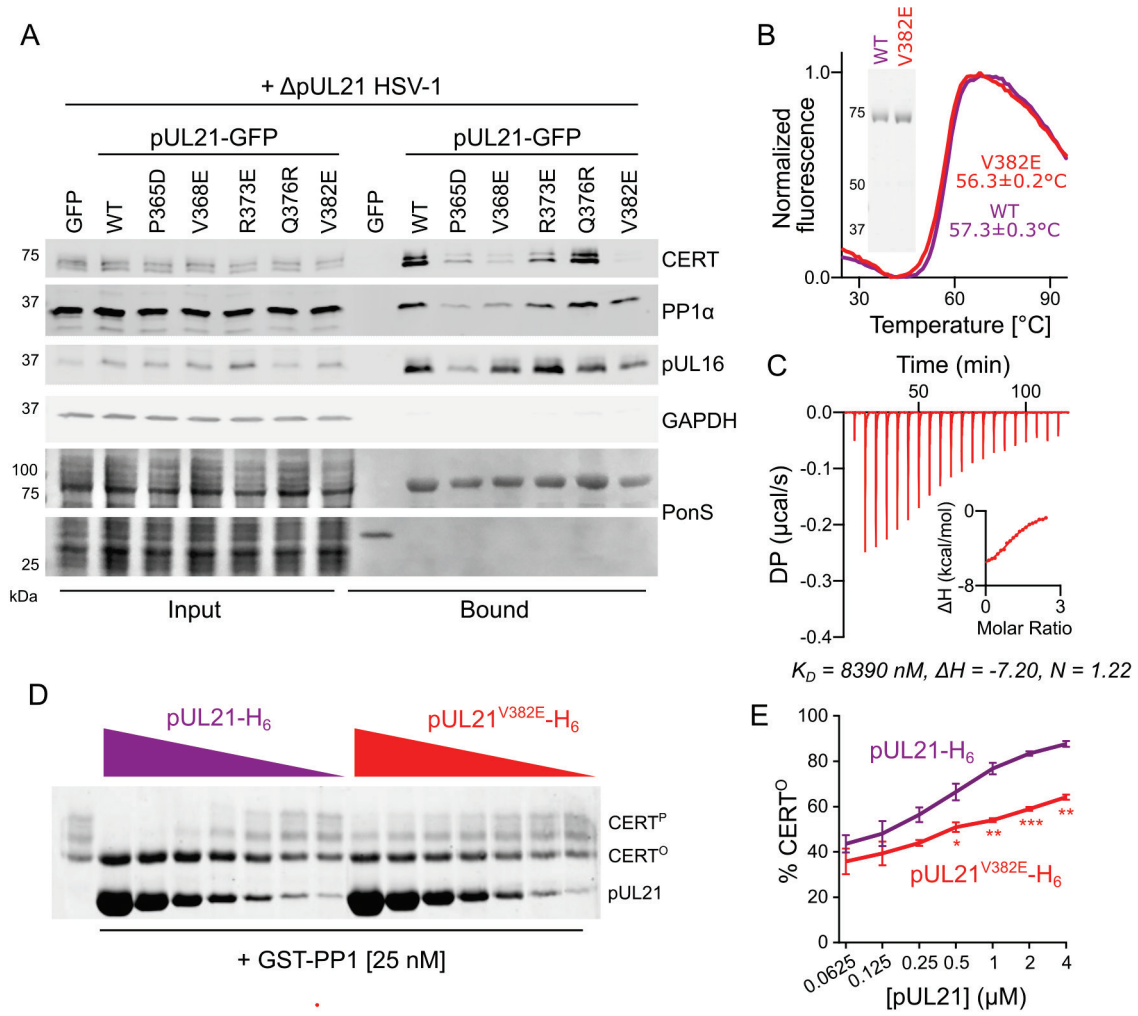

Figure 4. Identification and validation of a pUL21 point mutant with disrupted binding to CERT. (**A**) Immunoblot following immunoprecipitation from HEK293T cells transfected with plasmids encoding GFP-tagged pUL21, either wild-type (WT) or with amino acid substitutions at the putative $CERT_L$ binding interface (Fig 3H), or encoding GFP alone. At 24 hours post-transfection cells were infected with ΔpUL21 HSV-1 (MOI = 5) and at 16 hours post-infection cells were lysed, tagged proteins were captured using GFP affinity resin, and the bound proteins were subjected to SDS-PAGE and immunoblotting using the antibodies listed. Ponceau S (PonS) staining of the nitrocellulose membrane before blocking is shown to confirm efficient capture of GFP-tagged proteins. (**B**) Differential scanning fluorimetry of WT (purple) and V382E (red) pUL21-H_6. Representative curves are shown and melting temperature (T_m) is mean ± SEM of three technical replicates. Inset shows Coomassie-stained SDS-PAGE of the purified proteins. (**C**) Representative ITC titration curve of pUL21^{V382E}-H_6 binding to H_6-miniCERT$_L$. DP, differential power. Inset shows normalized binding curve with integrated changes in enthalpy (ΔH) as a function of molar ratio. The ranges of the vertical axes are identical to Fig 2F. The affinity (K_D), ΔH and stoichiometry (N) for the presented titration are displayed below. (**D**) *In vitro* dephosphorylation assay using all-purified proteins. 0.5 µM CERT^P was incubated with varying concentrations of pUL21-H_6 WT or V382E (two-fold dilution from 4 µM to 62.5 nM) in the presence of 25 nM GST-PP1 for 30 min at 30°C. Proteins were resolved using SDS-PAGE supplemented with PhosTag reagent to enhance

874 separation of CERT that is hyper- ($CERT^P$) or hypo-phosphorylated ($CERT^O$), and protein bands were
875 visualised using Coomassie. Images are representative of two independent experiments. (**E**)
876 Quantitation of concentration-dependent pUL21-mediated stimulation of CERT dephosphorylation as
877 determined by densitometry. Ratio of $CERT^O$ to total CERT ($CERT^O$+$CERT^P$) for two independent
878 experiments is shown (mean ± SEM). Data points are labelled if significantly different: *, $p < 0.05$; **, p
879 < 0.01; ***, $p < 0.001$ (two-way ANOVA with Sidak's multiple comparisons test)

880

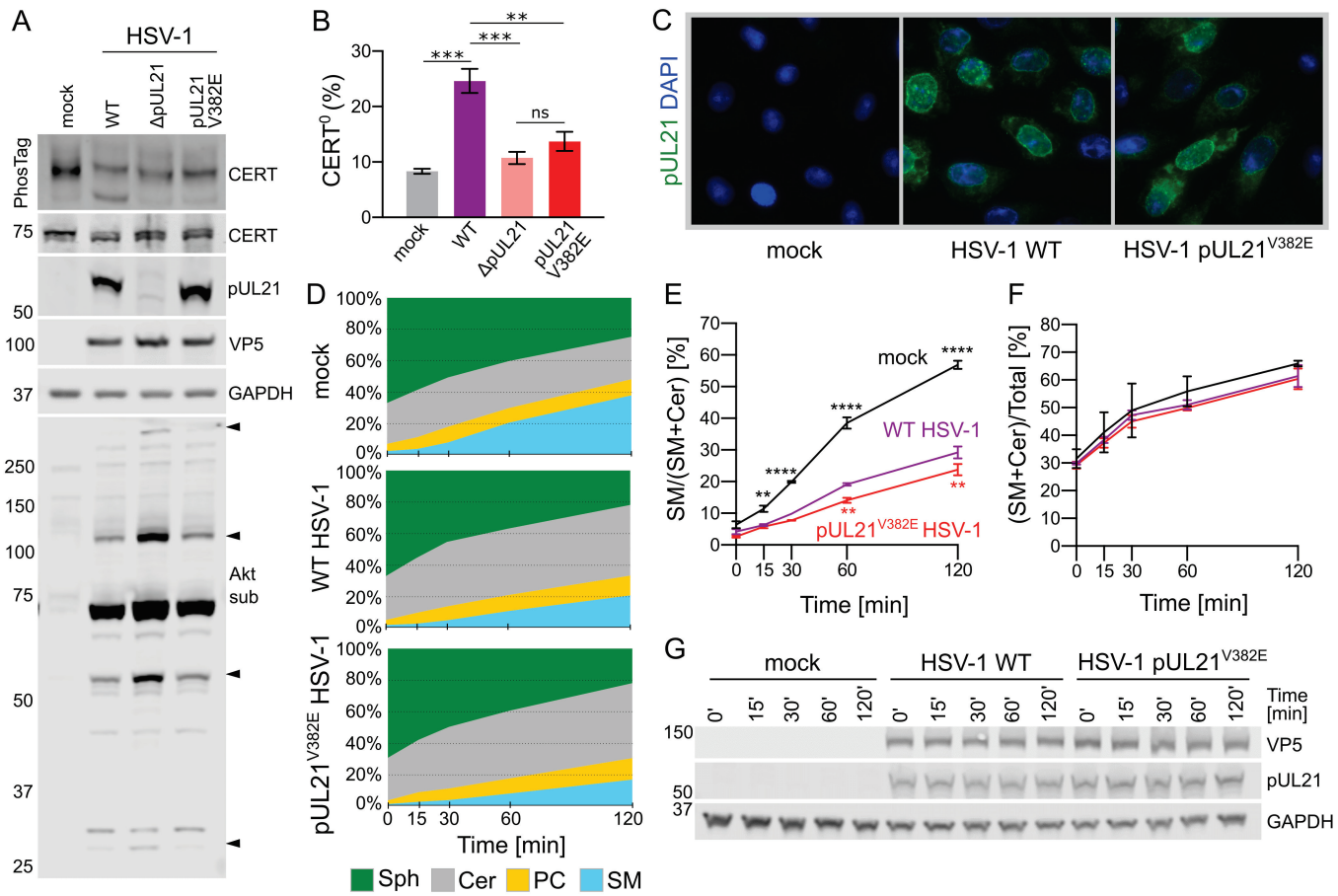

Figure 5. Mutating the CERT-binding interface of pUL21 inhibits CERT dephosphorylation and reduces the rate of sphingomyelin synthesis in infected cells. (**A**) HaCaT cells were infected at MOI = 5 with wild-type (WT) HSV-1, HSV-1 lacking pUL21 expression (ΔpUL21), or a pUL21 point mutant virus (pUL21^{V382E}). Lysates were harvested at 16 hpi in the presence of phosphatase inhibitors and subjected to SDS-PAGE plus immunoblotting using the antibodies listed. Where indicated, the gel was supplemented with PhosTag reagent to enhance separation of CERT phosphoforms. The antibody recognising phosphorylated Akt substrates (Akt sub) illustrates activity of the HSV-1 kinase pUS3, several substrates of which are dephosphorylated in a pUL21-dependent manner (arrowheads) [18]. VP5, infection control. (**B**) Quantitation of the CERT dephosphorylation level (ratio of CERT^{O} to total CERT) in cells infected with WT or mutant HSV-1, as determined by densitometry. Results are presented as mean ± SEM from three independent experiments. One-way ANOVA with Dunnett's multiple comparisons test was used for the statistical analysis (ns, non-significant; **, $p < 0.01$; ***, $p < 0.001$). (**C**) Vero cells were infected at MOI = 1, fixed 14 hpi and stained with DAPI (blue) plus an antibody recognising pUL21 (green). (**D**) Pulse-chase experiment to measure the rate of Sph conversion to Cer, SM and PC. HaCaT cells were infected with WT or pUL21^{V382E} HSV-1 at MOI = 5, or mock infected. Cells were incubated with 5 μM alkyne-Sph (pulse) at 14 hpi for 5 min and harvested for lipid extraction either immediately (0 min) or at the indicated times (chase). Extracted lipids were bioconjugated to 3-azido-7-hydroxycoumarin using click chemistry, separated by HPTLC, visualised using UV light and relative lipid abundances were quantitated by densitometry. Data is from one

900 representative experiment of two independent repeats. (**E**) Rate of SM synthesis expressed as its
901 fraction in the cumulative signal for SM and Cer. (**F**) The proportion of click-Sph incorporated into either
902 Cer or SM, representing the temporal influx of Sph into the SM biosynthesis pathway. For (**E**) and (**F**)
903 the data represents two independent experiments (mean ± SEM). Data points are labelled if significantly
904 different to WT HSV-1: **, $p < 0.01$; ****, $p < 0.0001$ (two-way ANOVA with Dunnett's multiple
905 comparisons test). (**G**) The re-solubilised proteins precipitated during lipid extraction were analysed by
906 SDS-PAGE and immunoblotting using the antibodies listed.

907

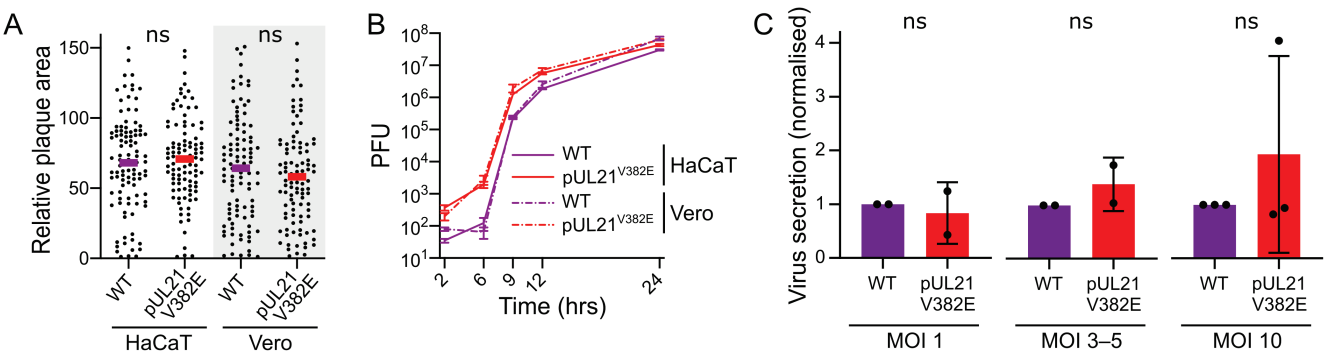

Figure 6. pUL21-mediated dephosphorylation of CERT accelerates virus replication but does not enhance virus secretion or cell-to-cell spread. (**A**) Monolayers of HaCaT or Vero cells were infected with 100 plaque forming units of WT or pUL21^{V382E} HSV-1. Following infection, cells were overlaid with medium containing 0.6% caboxymethyl cellulose and incubated for 48 hours, then fixed and immunostained with chromogenic detection. Relative plaque areas (pixels) were measured using Fiji [88,89]. Bars represent mean plaque sizes, which were compared using unpaired t-test (n=100; ns, non-significant). (**B**) Single-step (high MOI) growth curves of WT and pUL21^{V382E} HSV-1. Monolayers of HaCaT (continuous line) or Vero (dotted line) cells were infected (MOI = 5) with the viruses shown. Samples were harvested at the indicated times and titres determined by plaque assay using Vero cells. Data are presented as mean values ± SEM of technical duplicates from one representative experiment. Difference in replication kinetics across two biological replicates is not statistically significant (two-way ANOVA with Sidak's multiple comparisons test). (**C**) Virus release into the culture supernatant from HaCaT cells infected with WT or pUL21^{V382E} HSV-1 at various MOIs. Samples were harvested at 12 hpi and virus infectivity in the cells versus the culture medium was measured by titration on Vero cells. The fold change in secretion of infectivity into the culture medium for pUL21^{V382E} versus WT HSV-1 is shown as mean values ± SEM of two (MOI = 1 or 3–5) or three (MOI = 10) independent experiments. For MOI 3–5, the data represent one independent experiment performed at MOI = 3 and one at MOI = 5. For each MOI, the extent of virus secretion was compared using an unpaired t-test (ns, non-significant).

927 **Table 1. Thermodynamic properties of the pUL21:CERT$_L$ interaction**. As quantitated by isothermal
928 titration calorimetry (ITC). Experiments were performed *n* (replicates) times and mean ± SEM values
929 are shown.

Syringe	Cell	K_D [nM]	ΔH [kcal/mol]	ΔG [kcal/mol]	-TΔS [kcal/mol]	N (stoichiometry)	*n* (replicates)
CERT$_L^P$	pUL21	772.67 ± 158.18	3.89 ± 0.74	-8.37 ± 0.11	-12.27 ± 0.62	0.74 ± 0.01	3
CERT$_L^{S132A}$	pUL21	642.0 ± 182.0	2.385 ± 0.21	-8.475 ± 0.18	-10.85 ± 0.05	0.97 ± 0.04	2
miniCERT$_L$	pUL21	1042.0 ± 240.46	-8.65 ± 0.28	-8.21 ± 0.11	0.44 ± 0.35	0.89 ± 0.03	6
miniCERT$_L$	pUL21C	4325.0 ± 1175.0	-3.84 ± 0.02	-7.35 ± 0.17	-3.51 ± 0.18	0.97 ± 0.03	2
miniCERT$_L$	pUL21^{V382E}	8086.67 ± 538.53	-7.20 ± 0.03	-6.95 ± 0.04	0.26 ± 0.01	1.16 ± 0.08	3

930

931 **References**

932 1. Looker KJ, Magaret AS, May MT, Turner KME, Vickerman P, Gottlieb SL, et al. Global and
933 Regional Estimates of Prevalent and Incident Herpes Simplex Virus Type 1 Infections in 2012.
934 PloS One. 2015;10: e0140765. doi:10.1371/journal.pone.0140765

935 2. Kulej K, Avgousti DC, Sidoli S, Herrmann C, Fera AND, Kim ET, et al. Time-resolved Global and
936 Chromatin Proteomics during Herpes Simplex Virus Type 1 (HSV-1) Infection. Mol Cell
937 Proteomics MCP. 2017;16: S92. doi:10.1074/mcp.M116.065987

938 3. Soh TK, Davies CTR, Muenzner J, Hunter LM, Barrow HG, Connor V, et al. Temporal Proteomic
939 Analysis of Herpes Simplex Virus 1 Infection Reveals Cell-Surface Remodeling via pUL56-
940 Mediated GOPC Degradation. Cell Rep. 2020;33: 108235. doi:10.1016/j.celrep.2020.108235

941 4. Scherer KM, Manton JD, Soh TK, Mascheroni L, Connor V, Crump CM, et al. A fluorescent
942 reporter system enables spatiotemporal analysis of host cell modification during herpes simplex
943 virus-1 replication. J Biol Chem. 2021;296: 100236. doi:10.1074/jbc.RA120.016571

944 5. Nahas KL, Connor V, Scherer KM, Kaminski CF, Harkiolaki M, Crump CM, et al. Near-native state
945 imaging by cryo-soft-X-ray tomography reveals remodelling of multiple cellular organelles during
946 HSV-1 infection. PLoS Pathog. 2022;18: e1010629. doi:10.1371/journal.ppat.1010629

947 6. Bigalke JM, Heldwein EE. Nuclear Exodus: Herpesviruses Lead the Way. Annu Rev Virol. 2016;3:
948 387–409. doi:10.1146/annurev-virology-110615-042215

949 7. Owen DJ, Crump CM, Graham SC. Tegument Assembly and Secondary Envelopment of
950 Alphaherpesviruses. Viruses. 2015;7: 5084–5114. doi:10.3390/v7092861

951 8. Cocchi F, Menotti L, Dubreuil P, Lopez M, Campadelli-Fiume G. Cell-to-Cell Spread of Wild-Type
952 Herpes Simplex Virus Type 1, but Not of Syncytial Strains, Is Mediated by the Immunoglobulin-
953 Like Receptors That Mediate Virion Entry, Nectin1 (PRR1/HveC/HIgR) and Nectin2
954 (PRR2/HveB). J Virol. 2000;74: 3909–3917. doi:10.1128/JVI.74.8.3909-3917.2000

955 9. Le Sage V, Jung M, Alter JD, Wills EG, Johnston SM, Kawaguchi Y, et al. The herpes simplex
956 virus 2 UL21 protein is essential for virus propagation. J Virol. 2013;87: 5904–5915.
957 doi:10.1128/JVI.03489-12

958 10. Harper AL, Meckes DG, Marsh JA, Ward MD, Yeh P-C, Baird NL, et al. Interaction domains of the
959 UL16 and UL21 tegument proteins of herpes simplex virus. J Virol. 2010;84: 2963–2971.
960 doi:10.1128/JVI.02015-09

961 11. Klupp BG, Böttcher S, Granzow H, Kopp M, Mettenleiter TC. Complex formation between the
962 UL16 and UL21 tegument proteins of pseudorabies virus. J Virol. 2005;79: 1510–1522.
963 doi:10.1128/JVI.79.3.1510-1522.2005

964 12. Han J, Chadha P, Starkey JL, Wills JW. Function of glycoprotein E of herpes simplex virus
965 requires coordinated assembly of three tegument proteins on its cytoplasmic tail. Proc Natl Acad
966 Sci. 2012;109: 19798–19803. doi:10.1073/pnas.1212900109

967 13. Takakuwa H, Goshima F, Koshizuka T, Murata T, Daikoku T, Nishiyama Y. Herpes simplex virus
968 encodes a virion-associated protein which promotes long cellular processes in over-expressing
969 cells. Genes Cells. 2001;6: 955–966. doi:10.1046/j.1365-2443.2001.00475.x

970 14. Yan K, Liu J, Guan X, Yin Y-X, Peng H, Chen H-C, et al. The Carboxyl Terminus of Tegument
971 Protein pUL21 Contributes to Pseudorabies Virus Neuroinvasion. J Virol. 2019;93: 02052–18.
972 doi:10.1128/JVI.02052-18

973 15. Finnen RL, Banfield BW. CRISPR/Cas9 Mutagenesis of UL21 in Multiple Strains of Herpes
974 Simplex Virus Reveals Differential Requirements for pUL21 in Viral Replication. Viruses. 2018;10.
975 doi:10.3390/v10050258

976 16. Sarfo A, Starkey J, Mellinger E, Zhang D, Chadha P, Carmichael J, et al. The UL21 Tegument
977 Protein of Herpes Simplex Virus 1 Is Differentially Required for the Syncytial Phenotype. J Virol.
978 2017;91: 01161–17. doi:10.1128/JVI.01161-17

979 17. Klupp BG, Lomniczi B, Visser N, Fuchs W, Mettenleiter TC. Mutations affecting the UL21 gene
980 contribute to avirulence of pseudorabies virus vaccine strain Bartha. Virology. 1995;212: 466–
981 473. doi:10.1006/viro.1995.1504

982 18. Benedyk TH, Muenzner J, Connor V, Han Y, Brown K, Wijesinghe KJ, et al. pUL21 is a viral
983 phosphatase adaptor that promotes herpes simplex virus replication and spread. PLOS Pathog.
984 2021;17: e1009824. doi:10.1371/journal.ppat.1009824

985 19. Peti W, Nairn AC, Page R. Structural basis for protein phosphatase 1 regulation and specificity.
986 FEBS J. 2013;280: 596–611. doi:10.1111/j.1742-4658.2012.08509.x

987 20. Muradov JH, Finnen RL, Gulak MA, Hay TJM, Banfield BW. pUL21 regulation of pUs3 kinase
988 activity influences the nature of nuclear envelope deformation by the HSV-2 nuclear egress
989 complex. PLoS Pathog. 2021;17: e1009679. doi:10.1371/journal.ppat.1009679

990 21. Fukasawa M, Nishijima M, Hanada K. Genetic evidence for ATP-dependent endoplasmic
991 reticulum-to-Golgi apparatus trafficking of ceramide for sphingomyelin synthesis in Chinese
992 hamster ovary cells. J Cell Biol. 1999;144: 673–685. doi:10.1083/jcb.144.4.673

993 22. Funakoshi T, Yasuda S, Fukasawa M, Nishijima M, Hanada K. Reconstitution of ATP- and cytosol-
994 dependent transport of de novo synthesized ceramide to the site of sphingomyelin synthesis in
995 semi-intact cells. J Biol Chem. 2000;275: 29938–29945. doi:10.1074/jbc.M004470200

996 23. Hanada K, Kumagai K, Yasuda S, Miura Y, Kawano M, Fukasawa M, et al. Molecular machinery
997 for non-vesicular trafficking of ceramide. Nature. 2003;426: 803–809. doi:10.1038/nature02188

998 24. Prashek J, Truong T, Yao X. Crystal Structure of the Pleckstrin Homology Domain from the
999 Ceramide Transfer Protein: Implications for Conformational Change upon Ligand Binding. PLoS
1000 ONE. 2013;8: e79590. doi:10.1371/journal.pone.0079590

1001 25. Kudo N, Kumagai K, Tomishige N, Yamaji T, Wakatsuki S, Nishijima M, et al. Structural basis for
1002 specific lipid recognition by CERT responsible for nonvesicular trafficking of ceramide. Proc Natl
1003 Acad Sci. 2008;105: 488–493. doi:10.1073/pnas.0709191105

1004 26. Charruyer A, Bell SM, Kawano M, Douangpanya S, Yen T-Y, Macher BA, et al. Decreased
1005 Ceramide Transport Protein (CERT) Function Alters Sphingomyelin Production following UVB
1006 Irradiation. J Biol Chem. 2008;283: 16682–16692. doi:10.1074/jbc.M800799200

1007 27. Kawano M, Kumagai K, Nishijima M, Hanada K. Efficient trafficking of ceramide from the
1008 endoplasmic reticulum to the Golgi apparatus requires a VAMP-associated protein-interacting
1009 FFAT motif of CERT. J Biol Chem. 2006;281: 30279–30288. doi:10.1074/jbc.M605032200

1010 28. Kumagai K, Kawano M, Shinkai-Ouchi F, Nishijima M, Hanada K. Interorganelle trafficking of
1011 ceramide is regulated by phosphorylation-dependent cooperativity between the PH and START
1012 domains of CERT. J Biol Chem. 2007;282: 17758–17766. doi:10.1074/jbc.M702291200

1013 29. Hannun YA, Obeid LM. Sphingolipids and their metabolism in physiology and disease. Nat Rev
1014 Mol Cell Biol. 2018;19: 175–191. doi:10.1038/nrm.2017.107

1015 30. Sezgin E, Levental I, Mayor S, Eggeling C. The mystery of membrane organization: composition,
1016 regulation and roles of lipid rafts. Nat Rev Mol Cell Biol. 2017;18: 361–374.
1017 doi:10.1038/nrm.2017.16

1018 31. Olsen ASB, Faergeman NJ. Sphingolipids: membrane microdomains in brain development,
1019 function and neurological diseases. Open Biol. 2017;7: 170069. doi:10.1098/rsob.170069

1020 32. Elwell CA, Engel JN. Lipid acquisition by intracellular Chlamydiae. Cell Microbiol. 2012;14: 1010–
1021 1018. doi:10.1111/j.1462-5822.2012.01794.x

1022 33. Gewaid H, Aoyagi H, Arita M, Watashi K, Suzuki R, Sakai S, et al. Sphingomyelin Is Essential for
1023 the Structure and Function of the Double-Membrane Vesicles in Hepatitis C Virus RNA
1024 Replication Factories. J Virol. 2020;94: e01080-20. doi:10.1128/JVI.01080-20

1025 34. Ray EK, Blough HA. The effect of herpesvirus infection and 2-deoxy-d-glucose on
1026 glycosphingolipids in BHK-21 cells. Virology. 1978;88: 118–127. doi:10.1016/0042-
1027 6822(78)90115-0

1028 35. Steinhart WL, Busch JS, Oettgen JP, Howland JL. Sphingolipid metabolism during infection of
1029 human fibroblasts by herpes simplex virus type 1. Intervirology. 1984;21: 70–76.
1030 doi:10.1159/000149504

1031 36. Pastenkos G, Miller JL, Pritchard SM, Nicola AV. Role of Sphingomyelin in Alphaherpesvirus
1032 Entry. J Virol. 2019;93: e01547-18. doi:10.1128/JVI.01547-18

1033 37. Lang J, Bohn P, Bhat H, Jastrow H, Walkenfort B, Cansiz F, et al. Acid ceramidase of
1034 macrophages traps herpes simplex virus in multivesicular bodies and protects from severe
1035 disease. Nat Commun. 2020;11: 1338. doi:10.1038/s41467-020-15072-8

1036 38. Roussel E, Lippe R. Cellular Protein Kinase D Modulators Play a Role during Multiple Steps of
1037 Herpes Simplex Virus 1 Egress. J Virol. 2018;92: e01486-18. doi:10.1128/JVI.01486-18

1038 39. Shevchenko A, Simons K. Lipidomics: coming to grips with lipid diversity. Nat Rev Mol Cell Biol.
1039 2010;11: 593–598. doi:10.1038/nrm2934

1040 40. Sunshine H, Iruela-Arispe ML. Membrane Lipids and Cell Signaling. Curr Opin Lipidol. 2017;28:
1041 408–413. doi:10.1097/MOL.0000000000000443

1042 41. Gaebler A, Milan R, Straub L, Hoelper D, Kuerschner L, Thiele C. Alkyne lipids as substrates for
1043 click chemistry-based in vitro enzymatic assays. J Lipid Res. 2013;54: 2282–2290.
1044 doi:10.1194/jlr.D038653

1045 42. Gerl MJ, Bittl V, Kirchner S, Sachsenheimer T, Brunner HL, Lüchtenborg C, et al. Sphingosine-1-
1046 Phosphate Lyase Deficient Cells as a Tool to Study Protein Lipid Interactions. PLOS ONE.
1047 2016;11: e0153009. doi:10.1371/journal.pone.0153009

1048 43. Morash SC, Cook HW, Spence MW. Lysophosphatidylcholine as an intermediate in
1049 phosphatidylcholine metabolism and glycerophosphocholine synthesis in cultured cells: an
1050 evaluation of the roles of 1-acyl- and 2-acyl-lysophosphatidylcholine. Biochim Biophys Acta.
1051 1989;1004: 221–229. doi:10.1016/0005-2760(89)90271-3

1052 44. Yasuda S, Kitagawa H, Ueno M, Ishitani H, Fukasawa M, Nishijima M, et al. A Novel Inhibitor of
1053 Ceramide Trafficking from the Endoplasmic Reticulum to the Site of Sphingomyelin Synthesis. J
1054 Biol Chem. 2001;276: 43994–44002. doi:10.1074/jbc.M104884200

1055 45. Prischi F, Filippakopoulos P. Editorial: Structural Studies of Protein Complexes in Signaling
1056 Pathways. Front Mol Biosci. 2021;8: 200. doi:10.3389/fmolb.2021.641932

1057 46. Prashek J, Bouyain S, Fu M, Li Y, Berkes D, Yao X. Interaction between the PH and START
1058 domains of ceramide transfer protein competes with phosphatidylinositol 4-phosphate binding by
1059 the PH domain. J Biol Chem. 2017;292: 14217–14228. doi:10.1074/jbc.M117.780007

1060 47. Sugiki T, Takeuchi K, Yamaji T, Takano T, Tokunaga Y, Kumagai K, et al. Structural Basis for the
1061 Golgi Association by the Pleckstrin Homology Domain of the Ceramide Trafficking Protein
1062 (CERT). J Biol Chem. 2012;287: 33706–33718. doi:10.1074/jbc.M112.367730

1063 48. Raya A, Revert-Ros F, Martinez-Martinez P, Navarro S, Roselló E, Vieites B, et al. Goodpasture
1064 Antigen-binding Protein, the Kinase That Phosphorylates the Goodpasture Antigen, Is an
1065 Alternatively Spliced Variant Implicated in Autoimmune Pathogenesis. J Biol Chem. 2000;275:
1066 40392–40399. doi:10.1074/jbc.M002769200

1067 49. Svergun DI, Petoukhov MV, Koch MHJ. Determination of Domain Structure of Proteins from X-
1068 Ray Solution Scattering. Biophys J. 2001;80: 2946–2953. doi:10.1016/S0006-3495(01)76260-1

1069 50. Metrick CM, Heldwein EE. Novel Structure and Unexpected RNA-Binding Ability of the C-Terminal
1070 Domain of Herpes Simplex Virus 1 Tegument Protein UL21. J Virol. 2016;90: 5759–5769.
1071 doi:10.1128/JVI.00475-16

1072 51. Metrick CM, Chadha P, Heldwein EE. The unusual fold of herpes simplex virus 1 UL21, a
1073 multifunctional tegument protein. J Virol. 2015;89: 2979–2984. doi:10.1128/JVI.03516-14

1074 52. Tischer BK, Smith GA, Osterrieder N. En passant mutagenesis: a two step markerless red
1075 recombination system. Methods Mol Biol Clifton NJ. 2010;634: 421–430. doi:10.1007/978-1-
1076 60761-652-8_30

1077 53. Chuluunbaatar U, Roller R, Feldman ME, Brown S, Shokat KM, Mohr I. Constitutive mTORC1
1078 activation by a herpesvirus Akt surrogate stimulates mRNA translation and viral replication. Genes
1079 Dev. 2010;24: 2627–2639. doi:10.1101/gad.1978310

1080 54. Roussel É, Lippé R. Cellular Protein Kinase D Modulators Play a Role during Multiple Steps of
1081 Herpes Simplex Virus 1 Egress. J Virol. 2018;92: e01486-18. doi:10.1128/JVI.01486-18

1082 55. Bell C, Desjardins M, Thibault P, Radtke K. Proteomics analysis of herpes simplex virus type 1-
1083 infected cells reveals dynamic changes of viral protein expression, ubiquitylation, and
1084 phosphorylation. J Proteome Res. 2013;12: 1820–1829. doi:10.1021/pr301157j

1085 56. Langeland N, Haarr L, Holmsen H. Polyphosphoinositide metabolism in baby-hamster kidney cells
1086 infected with herpes simplex virus type 1. Biochem J. 1986;237: 707–712. doi:10.1042/bj2370707

1087 57. Sutter E, de Oliveira AP, Tobler K, Schraner EM, Sonda S, Kaech A, et al. Herpes simplex virus
1088 1 induces de novo phospholipid synthesis. Virology. 2012;429: 124–135.
1089 doi:10.1016/j.virol.2012.04.004

1090 58. Han X. Lipidomics for studying metabolism. Nat Rev Endocrinol. 2016;12: 668–679.
1091 doi:10.1038/nrendo.2016.98

1092 59. Xu T, Hu C, Xuan Q, Xu G. Recent advances in analytical strategies for mass spectrometry-based
1093 lipidomics. Anal Chim Acta. 2020;1137: 156–169. doi:10.1016/j.aca.2020.09.060

1094 60. Campadelli G, Brandimarti R, Lazzaro CD, Ward PL, Roizman B, Torrisi MR. Fragmentation and
1095 dispersal of Golgi proteins and redistribution of glycoproteins and glycolipids processed through
1096 the Golgi apparatus after infection with herpes simplex virus 1. Proc Natl Acad Sci. 1993;90:
1097 2798–2802. doi:10.1073/pnas.90.7.2798

1098 61. Kumagai K, Hanada K. Structure, functions and regulation of CERT, a lipid-transfer protein for the
1099 delivery of ceramide at the ER-Golgi membrane contact sites. FEBS Lett. 2019;593: 2366–2377.
1100 doi:10.1002/1873-3468.13511

1101 62. Rémillard-Labrosse G, Mihai C, Duron J, Guay G, Lippé R. Protein kinase D-dependent trafficking
1102 of the large Herpes simplex virus type 1 capsids from the TGN to plasma membrane. Traffic Cph
1103 Den. 2009;10: 1074–1083. doi:10.1111/j.1600-0854.2009.00939.x

1104 63. Alonso A, Goñi FM. The Physical Properties of Ceramides in Membranes. Annu Rev Biophys.
1105 2018;47: 633–654. doi:10.1146/annurev-biophys-070317-033309

1106 64. Bigalke JM, Heldwein EE. Structural basis of membrane budding by the nuclear egress complex
1107 of herpesviruses. EMBO J. 2015;34: 2921–2936. doi:10.15252/embj.201592359

1108 65. Thorsen MK, Lai A, Lee MW, Hoogerheide DP, Wong GCL, Freed JH, et al. Highly Basic Clusters
1109 in the Herpes Simplex Virus 1 Nuclear Egress Complex Drive Membrane Budding by Inducing
1110 Lipid Ordering. mBio. 12: e01548-21. doi:10.1128/mBio.01548-21

1111 66. Ogretmen B. Sphingolipid metabolism in cancer signalling and therapy. Nat Rev Cancer. 2018;18:
1112 33–50. doi:10.1038/nrc.2017.96

1113 67. Galvan V, Roizman B. Herpes simplex virus 1 induces and blocks apoptosis at multiple steps
1114 during infection and protects cells from exogenous inducers in a cell-type-dependent manner.
1115 Proc Natl Acad Sci U S A. 1998;95: 3931–3936. doi:10.1073/pnas.95.7.3931

1116 68. Li Z, Michael IP, Zhou D, Nagy A, Rini JM. Simple piggyBac transposon-based mammalian cell
1117 expression system for inducible protein production. Proc Natl Acad Sci U S A. 2013;110: 5004–
1118 5009. doi:10.1073/pnas.1218620110

1119 69. Zufferey R, Donello JE, Trono D, Hope TJ. Woodchuck hepatitis virus posttranscriptional
1120 regulatory element enhances expression of transgenes delivered by retroviral vectors. J Virol.
1121 1999;73: 2886–2892. doi:10.1128/JVI.73.4.2886-2892.1999

1122 70. Neidel S, Maluquer de Motes C, Mansur DS, Strnadova P, Smith GL, Graham SC. Vaccinia virus
1123 protein A49 is an unexpected member of the B-cell Lymphoma (Bcl)-2 protein family. J Biol Chem.
1124 2015;290: 5991–6002. doi:10.1074/jbc.M114.624650

1125 71. Chen R, Rato C, Yan Y, Crespillo-Casado A, Clarke HJ, Harding HP, et al. G-actin provides
1126 substrate-specificity to eukaryotic initiation factor 2α holophosphatases. eLife. 2015;4.
1127 doi:10.7554/eLife.04871

1128 72. Boukamp P, Petrussevska RT, Breitkreutz D, Hornung J, Markham A, Fusenig NE. Normal
1129 keratinization in a spontaneously immortalized aneuploid human keratinocyte cell line. J Cell Biol.
1130 1988;106: 761–771. doi:10.1083/jcb.106.3.761

1131 73. Carmichael JC, Wills JW. Differential Requirements for gE, gI, and UL16 among Herpes Simplex
1132 Virus 1 Syncytial Variants Suggest Unique Modes of Dysregulating the Mechanism of Cell-to-Cell
1133 Spread. J Virol. 2019;93. doi:10.1128/JVI.00494-19

1134 74. McClelland DA, Aitken JD, Bhella D, McNab D, Mitchell J, Kelly SM, et al. pH reduction as a trigger
1135 for dissociation of herpes simplex virus type 1 scaffolds. J Virol. 2002;76: 7407–7417.
1136 doi:10.1128/jvi.76.15.7407-7417.2002

1137 75. Minson AC, Hodgman TC, Digard P, Hancock DC, Bell SE, Buckmaster EA. An analysis of the
1138 biological properties of monoclonal antibodies against glycoprotein D of herpes simplex virus and
1139 identification of amino acid substitutions that confer resistance to neutralization. J Gen Virol.
1140 1986;67: 1001–1013. doi:10.1099/0022-1317-67-6-1001

76. Gierasch WW, Zimmerman DL, Ward SL, VanHeyningen TK, Romine JD, Leib DA. Construction and characterization of bacterial artificial chromosomes containing HSV-1 strains 17 and KOS. J Virol Methods. 2006;135: 197–206. doi:10.1016/j.jviromet.2006.03.014

77. Blanchet CE, Spilotros A, Schwemmer F, Graewert MA, Kikhney A, Jeffries CM, et al. Versatile sample environments and automation for biological solution X-ray scattering experiments at the P12 beamline (PETRA III, DESY). J Appl Crystallogr. 2015;48: 431–443. doi:10.1107/S160057671500254X

78. Graewert MA, Franke D, Jeffries CM, Blanchet CE, Ruskule D, Kuhle K, et al. Automated pipeline for purification, biophysical and x-ray analysis of biomacromolecular solutions. Sci Rep. 2015;5: 10734. doi:10.1038/srep10734

79. Wilkins MR, Gasteiger E, Bairoch A, Sanchez JC, Williams KL, Appel RD, et al. Protein identification and analysis tools in the ExPASy server. Methods Mol Biol Clifton NJ. 1999;112: 531–552. doi:10.1385/1-59259-584-7:531

80. Panjkovich A, Svergun DI. CHROMIXS: automatic and interactive analysis of chromatography-coupled small-angle X-ray scattering data. Bioinformatics. 2018;34: 1944–1946. doi:10.1093/bioinformatics/btx846

81. Franke D, Jeffries CM, Svergun DI. Correlation Map, a goodness-of-fit test for one-dimensional X-ray scattering spectra. Nat Methods. 2015;12: 419–422. doi:10.1038/nmeth.3358

82. Manalastas-Cantos K, Konarev PV, Hajizadeh NR, Kikhney AG, Petoukhov MV, Molodenskiy DS, et al. ATSAS 3.0: expanded functionality and new tools for small-angle scattering data analysis. J Appl Crystallogr. 2021;54: 343–355. doi:10.1107/S1600576720013412

83. Svergun DI. Determination of the regularization parameter in indirect-transform methods using perceptual criteria. J Appl Crystallogr. 1992;25: 495–503. doi:10.1107/S0021889892001663

84. Hajizadeh NR, Franke D, Jeffries CM, Svergun DI. Consensus Bayesian assessment of protein molecular mass from solution X-ray scattering data. Sci Rep. 2018;8: 7204. doi:10.1038/s41598-018-25355-2

85. Petoukhov MV, Franke D, Shkumatov AV, Tria G, Kikhney AG, Gajda M, et al. New developments in the ATSAS program package for small-angle scattering data analysis. J Appl Crystallogr. 2012;45: 342–350. doi:10.1107/S0021889812007662

86. Yang J, Yan R, Roy A, Xu D, Poisson J, Zhang Y. The I-TASSER Suite: protein structure and function prediction. Nat Methods. 2015;12: 7–8. doi:10.1038/nmeth.3213

87. Svergun D, Barberato C, Koch MHJ. *CRYSOL* – a Program to Evaluate X-ray Solution Scattering of Biological Macromolecules from Atomic Coordinates. J Appl Crystallogr. 1995;28: 768–773. doi:10.1107/S0021889895007047

88. Rueden CT, Schindelin J, Hiner MC, DeZonia BE, Walter AE, Arena ET, et al. ImageJ2: ImageJ for the next generation of scientific image data. BMC Bioinformatics. 2017;18: 529. doi:10.1186/s12859-017-1934-z

89. Schindelin J, Arganda-Carreras I, Frise E, Kaynig V, Longair M, Pietzsch T, et al. Fiji: an open-source platform for biological-image analysis. Nat Methods. 2012;9: 676–682. doi:10.1038/nmeth.2019

90. Valentini E, Kikhney AG, Previtali G, Jeffries CM, Svergun DI. SASBDB, a repository for biological small-angle scattering data. Nucleic Acids Res. 2015;43: D357-363. doi:10.1093/nar/gku1047

1183 91. Receveur-Brechot V, Durand D. How random are intrinsically disordered proteins? A small angle
1184 scattering perspective. Curr Protein Pept Sci. 2012;13: 55–75.
1185 doi:10.2174/138920312799277901

1186